

Article

Analysis of the Polarization Distribution and Spin Angular Momentum of the Interference Field Obtained by Co-Planar Beams with Linear and Circular Polarization

Svetlana N. Khonina ^{1,2,*} , Andrey V. Ustinov ², Alexey P. Porfirev ^{1,2} and Sergey V. Karpeev ^{1,2}

¹ Scientific Research Laboratory of Automated Systems of Scientific Research (SRL-35), Samara National Research University, Moskovskoye Shosse 34, 443086 Samara, Russia; porfirev.alexey@ipsiras.ru (A.P.P.); karp@ipsiras.ru (S.V.K.)

² Image Processing Systems Institute, National Research Centre “Kurchatov Institute”, Molodogvardeyskaya Str. 151, 443001 Samara, Russia; andr@ipsiras.ru

* Correspondence: khonina@ipsiras.ru

Abstract: Interference of two and four light beams with linear or circular polarization is studied analytically and numerically based on the Richards–Wolf formalism. We consider such characteristics of the interference fields as the distribution of intensity, polarization, and spin angular momentum density. The generation of light fields with 1D and 2D periodic structure of both intensity and polarization is demonstrated. We can control the periodic structure both by changing the polarization state of the interfering beams and by changing the numerical aperture of focusing. We consider examples with a basic configuration, as well as those with a certain symmetry in the polarization state of the interfering beams. In some cases, increasing the numerical aperture of the focusing system significantly affects the generated distributions of both intensity and polarization. Experimental results, obtained using a polarization video camera, are in good agreement with the simulation results. The considered light fields can be used in laser processing of thin films of photosensitive (as well as polarization-sensitive) materials in order to create arrays of various ordered nano- and microstructures.

Keywords: polarization; multi-beam interference; circular polarization; linear polarization; Richards–Wolf formulas



Citation: Khonina, S.N.; Ustinov, A.V.; Porfirev, A.P.; Karpeev, S.V. Analysis of the Polarization Distribution and Spin Angular Momentum of the Interference Field Obtained by Co-Planar Beams with Linear and Circular Polarization. *Photonics* **2024**, *11*, 478. <https://doi.org/10.3390/photonics11050478>

Received: 20 April 2024

Revised: 17 May 2024

Accepted: 17 May 2024

Published: 19 May 2024



Copyright: © 2024 by the authors. Licensee MDPI, Basel, Switzerland. This article is an open access article distributed under the terms and conditions of the Creative Commons Attribution (CC BY) license (<https://creativecommons.org/licenses/by/4.0/>).

1. Introduction

Currently, light fields with a nonuniform polarization state are increasingly used to solve problems of optical microscopy, laser processing of materials, laser manipulation, holography, and optical communications [1–4]. To form such structured light fields, it is necessary to use subwavelength gratings that are quite complex to manufacture [5], metasurfaces [6] and metalenses [7], or approaches based on the mode addition of two orthogonally polarized light fields [8]. The last of the mentioned approaches is implemented both with the help of dynamic spatial light modulators (SLMs) [9] and with the help of diffractive optical elements (DOEs) [10]. The DOEs have a high damage threshold that allows them to be used with powerful laser pulses; however, DOEs are inferior in functionality to modern SLMs and in most cases are more demanding for adjustment. Relatively simple profiles of nonuniformly polarized light fields can be formed using various sector polarizing plates that consist of either rotated polarizing films or birefringent crystals with rotated axes [11]. The disadvantages of such elements include the occurrence of diffraction effects at the junctions of sectors, as well as a relatively small set of types of inhomogeneously polarized fields that can be formed with their help. Also, the quality of the generated fields is significantly lower compared to the methods based on subwavelength gratings.

At the same time, there are quite simple methods for generating non-uniformly polarized light fields with a periodically repeating structure. Such structured light fields are especially interesting in laser processing of materials and laser manipulation, since they

can significantly speed up the processing or provide trapping and moving many nano- and micro-objects [12,13]. These approaches include the method of multi-beam interference of linearly or circularly polarized beams. In this case, by changing the polarization states of the beams or their locations, it is possible to form different polarization profiles with a periodicity depending on the angle of convergence of the beams. This approach does not require the use of special optical elements but provides ample opportunities for dynamic control of the field polarization structure.

It was previously shown that using two or more interfering beams with specified properties, one can quickly form two-dimensional or three-dimensional diffraction structures in photosensitive materials [14–20]. Moreover, studies of the influence of the polarization state of various beams on the formation of relief in polarization-sensitive materials are increasingly appearing [21–26].

Most works analyze the influence of the geometric arrangement of interfering beams and their polarization state on the contrast of the formed relief [27–30]. In this case, the TE- or TM-polarization of beams is often considered with respect to the radius vector connecting the origin of the input plane and the center of the position of the corresponding beam. Thus, with multi-beam interference, the influence of linear polarization with a certain configuration is studied. Note that the best contrast in lithography was predicted for structures formed by coplanar (diametrically spaced relative to the origin) pairs of beams [24,29,30] with TE polarization corresponding to the azimuthal configuration. When structuring polarization-sensitive materials, better contrast is achieved due to the interference of beams with orthogonal circular or diagonal polarizations, depending on the polymer type [23–26].

In this work, we analyze the influence of various combinations of polarization not only on the distribution of vector field intensity interference (for each component) but also on the distribution of the polarization state, as well as on the spin angular momentum (SAM) density.

Analytical expressions were obtained for the interference of two and four beams from point sources in the Richards–Wolf formalism [31,32]. This made it possible to show the difference between paraxial approximation and sharp focusing for several special cases that are important in the structuring of polarization-sensitive materials.

2. Methods

Theoretical Background

We consider a set of point sources $F_p(x, y)$, implemented, for example, as holes in a black screen, and having a certain type of polarization $\mathbf{c}_p = (c_{xp}, c_{yp})^T$:

$$\mathbf{F}(x, y) = \sum_{p=1}^P \mathbf{c}_p F_p(x, y) = \sum_{p=1}^P \mathbf{c}_p a_p \delta(x - x_p, y - y_p) \quad (1)$$

where $\delta(x, y)$ is the delta function, and a_p is the weight coefficient (complex in the general case).

It is known that when propagating in the far zone, radiation from a set of point sources corresponds to a superposition of plane waves [33]. Therefore, as a rule, the interference of plane waves created by a set of point sources (or small holes) is considered [27–30,33–38]. However, field 1 can also be focused using both conventional lenses and objective lenses.

When radiation interacts with matter, not only is the amplitude-phase distribution of the field near the irradiated surface important but also the polarization state [39–41], as well as the component ratio [42–44].

The components of the electric field vectors when focusing each point source can be calculated using the Richards–Wolf formulas [31,32]:

$$\mathbf{E}_p(r, \varphi, z) = -\frac{if}{\lambda} \int_0^\alpha \int_0^{2\pi} T(\theta) F_p(\theta, \phi) \mathbf{P}_p(\theta, \phi) \exp[ik(r \sin \theta \cos(\phi - \varphi) + z \cos \theta)] \sin \theta d\theta d\phi \quad (2)$$

where

$$\mathbf{P}_p(\theta, \phi) = \begin{bmatrix} A(\theta, \phi) & C(\theta, \phi) \\ C(\theta, \phi) & B(\theta, \phi) \\ -D(\theta, \phi) & -E(\theta, \phi) \end{bmatrix} \begin{pmatrix} c_{xp}(\theta, \phi) \\ c_{yp}(\theta, \phi) \end{pmatrix}. \quad (3)$$

Expression (3) uses the following notation:

$$\begin{aligned} A(\theta, \phi) &= 1 + \cos^2 \phi (\cos \theta - 1), \\ B(\theta, \phi) &= 1 + \sin^2 \phi (\cos \theta - 1), \\ C(\theta, \phi) &= \sin \phi \cos \phi (\cos \theta - 1), \\ D(\theta, \phi) &= \cos \phi \sin \theta, \\ E(\theta, \phi) &= \sin \phi \sin \theta. \end{aligned} \quad (4)$$

In Expressions (2)–(4) (r, ϕ, z) are cylindrical coordinates in the focal region, (θ, ϕ) are spherical angular coordinates at the exit of the pupil of the focusing system, $\sin(\alpha) = \text{NA}$ is the numerical aperture of the system, $F_p(\theta, \phi)$ is the transmission (input) function, $T(\theta)$ is the apodization function, $k = 2\pi/\lambda$ is the wave number, λ is the radiation wavelength, and f is the focal length (see Figure 1).

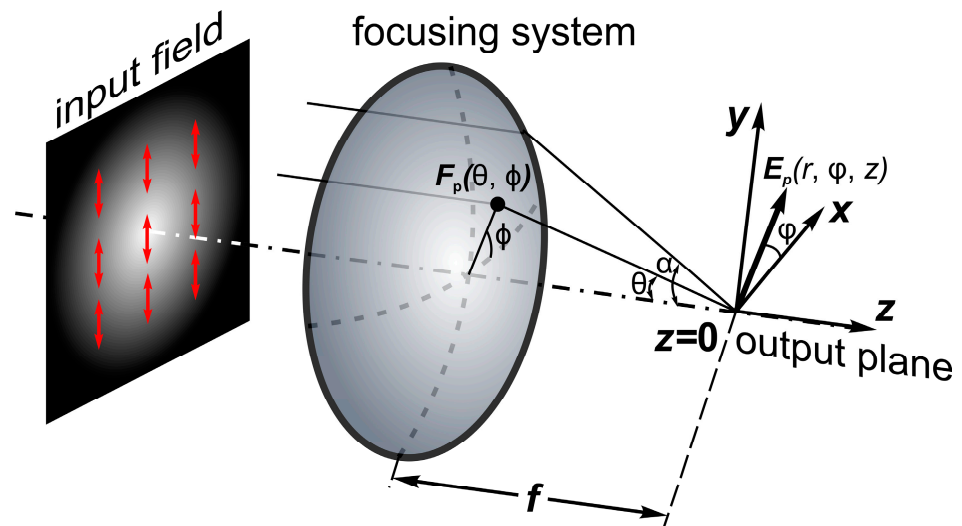


Figure 1. Explanations for the Richards–Wolf formulas: focusing a linearly polarized beam through a lens with focal length f and maximum azimuthal angle α .

In spherical coordinates, field 1 will take the following form:

$$\mathbf{F}(\theta, \phi) = \sum_{p=1}^P \mathbf{c}_p F_p(\theta, \phi) = \sum_{p=1}^P \mathbf{c}_p a_p \delta(\theta - \theta_p, \phi - \phi_p) \quad (5)$$

Further, for symmetry reasons, we shall assume that the set of points in Expression (5) is located on a ring with radius $f \sin \theta_0$. Then, Function (5) depends only on the angle ϕ :

$$\mathbf{F}(\phi) = \delta(\theta - \theta_0) \sum_{p=1}^P \mathbf{c}_p F(\phi_p) = \delta(\theta - \theta_0) \sum_{p=1}^P \mathbf{c}_p a_p \delta(\phi - \phi_p) \quad (6)$$

When substituting Expressions (5) or (6) into Formula (2), due to the filtering action of the delta functions, the integration operation disappears [45,46]. So, in this case, the total field after focusing will be the result of a superposition of fields in Equation (2):

$$\mathbf{E}(r, \phi, z) = -\frac{if}{\lambda} \sum_{p=1}^P A_p \mathbf{E}_p(r, \phi, z) \quad (7)$$

where $A_p = a_p T(\theta_0) \sin(\theta_0)$.

In this work, we are interested in the result in the focal plane ($z = 0$). In this case, the result of focusing for each individual source can be written explicitly for all components of the electric field:

$$\begin{aligned} E_{xp}(r, \varphi, 0) &= F(\phi_p) \left\{ \left[1 - \cos^2 \phi_p (1 - \cos \theta_0) \right] c_{xp} - \sin \phi_p \cos \phi_p (1 - \cos \theta_0) c_{yp} \right\} \exp \left[ikr \sin \theta_0 \cos(\phi_p - \varphi) \right], \\ E_{yp}(r, \varphi, 0) &= F(\phi_p) \left\{ \left[1 - \sin^2 \phi_p (1 - \cos \theta_0) \right] c_{yp} - \sin \phi_p \cos \phi_p (1 - \cos \theta_0) c_{xp} \right\} \exp \left[ikr \sin \theta_0 \cos(\phi_p - \varphi) \right], \\ E_{zp}(r, \varphi, 0) &= F(\phi_p) \left[-\sin \theta_0 (c_{xp} \cos \phi_p + c_{yp} \sin \phi_p) \right] \exp \left[ikr \sin \theta_0 \cos(\phi_p - \varphi) \right]. \end{aligned} \quad (8)$$

From Expression (8) it is clear that a significant change in the distribution of field components is possible due to the polarization state of each source $\mathbf{c}_p = (c_{xp}, c_{yp})^T$ (even in the case of the accepted symmetry condition of Equation (6)).

In this work, we shall consider for field 7, formed by the interference of two or more beams of Expression (8), such characteristics as the distribution of intensity, polarization, and SAM density.

The SAM density distribution may be calculated by the following formula [47]:

$$\mathbf{s}(r, \varphi, z) \simeq \text{Im}[\mathbf{E}^*(r, \varphi, z) \times \mathbf{E}(r, \varphi, z)]. \quad (9)$$

The individual components of the SAM density distribution are defined as follows:

$$\mathbf{s}(r, \varphi, z) = \begin{pmatrix} s_x \\ s_y \\ s_z \end{pmatrix} \simeq \text{Im} \begin{pmatrix} E_y^* E_z - E_z^* E_y \\ E_z^* E_x - E_x^* E_z \\ E_x^* E_y - E_y^* E_x \end{pmatrix}. \quad (10)$$

It is well known that the longitudinal component of the SAM s_z is associated with the presence of circular polarization in the generated field [48–51], which allows trapped particles to rotate around their axis in the transverse plane. In the paraxial case, the longitudinal component of the SAM dominates the transverse components. However, with sharp focusing, especially of structured beams, transverse components of the SAM may also be present [52–55], which ensures the rotation of the particles around their axis in the direction of the light propagation. The presence of both transverse and longitudinal components [56] can lead to complex 3D rotation of trapped particles.

Next, we shall consider some special cases and modeling results illustrating them both in the paraxial case and with sharp focusing.

3. Analysis and Modeling Results for Interfering Beams

Obviously, the simplest case is the interference of two beams. However, if we add two expressions of Expression (8) for *arbitrary* ϕ_1 and ϕ_2 , then the general field will not have interesting properties. Therefore, we consider a superposition with a certain symmetry also along the angle ϕ .

3.1. Superposition of Two Horizontally Spaced Beams

Let us consider the simplest case for analytical calculations, when $\phi_1 = 0^\circ$, $\phi_2 = 180^\circ$. Note that the result will be similar for any pair of diametrically opposite (coplanar) points up to rotation.

For two *horizontally* spaced beams we obtain:

$$\begin{aligned} E_x &= \cos \theta_0 [c_{x1} \exp(i\alpha x) + c_{x2} \exp(-i\alpha x)], \\ E_y &= c_{y1} \exp(i\alpha x) + c_{y2} \exp(-i\alpha x), \\ E_z &= -\sin \theta_0 [c_{x1} \exp(i\alpha x) + c_{x2} \exp(-i\alpha x)]. \end{aligned} \quad (11)$$

To obtain Expression (11), we use the notation $\alpha = k \sin \theta_0$, reduction formulas, and the equalities $x = r \cos \varphi$, $y = r \sin \varphi$. From Expression (11), it is clear that the dependences

of all three components are *one-dimensional*: only on variable x . Thus, a one-dimensional lattice is formed. In addition, it can be noted that the x - and z -components of the field depend only on the x -component of the initial polarization vector, and the y -component depends only on the initial y -component.

The interference of two beams with different polarizations is often used to study the photo-induced properties of materials when forming one-dimensional gratings with different contrasts [23–26].

Below, we give several examples with different polarization vectors. When modeling, instead of pinholes in a black screen, we used a set of Gaussian beams: $G(x, y) = \exp(-(x^2 + y^2)/\sigma^2)$. In the case when the radius of the Gaussian beam σ is small compared to the total size of the input field, such a replacement does not introduce significant differences compared to the theoretical model with point sources [57,58]. But such an approximation is more convenient for numerical calculations.

Calculation parameters: wavelength is $\lambda = 1 \mu\text{m}$, input field size is $200 \times 200 \mu\text{m}$, and $\sigma = 10 \mu\text{m}$. In the paraxial case, the numerical aperture is $\text{NA} = 0.15$, and the output field size is $16 \times 16 \mu\text{m}$. With sharp focusing, numerical aperture $\text{NA} = 0.99$, and output field size is $4 \times 4 \mu\text{m}$.

3.1.1. Two Beams with the Same Polarization: $\mathbf{c}_2 = \begin{bmatrix} c_{x2} \\ c_{y2} \end{bmatrix} = \mathbf{c}_1 = \begin{bmatrix} c_{x1} \\ c_{y1} \end{bmatrix}$

With the same polarization vectors in both beams, the expressions become especially simple thanks to Euler’s formulas. When substituting into Expression (9), we get:

$$\begin{aligned} E_x &= 2c_{x1} \cos \theta_0 \cos(\alpha x), \\ E_y &= 2c_{y1} \cos(\alpha x), \\ E_z &= -2c_{x1}i \sin \theta_0 \sin(\alpha x). \end{aligned} \tag{12}$$

Taking into account paraxiality ($\cos\theta_0 \approx 1$, $\sin\theta_0 \approx 0$), Expression (12) is reduced to an even simpler form:

$$\begin{aligned} E_x &\approx 2c_{x1} \cos(\alpha x), \\ E_y &= 2c_{y1} \cos(\alpha x), \\ E_z &\approx 0. \end{aligned} \tag{13}$$

From Expression (13), it is clear that an amplitude grating is formed, the period of which increases in inverse proportion to the value $\alpha = k \sin\theta_0$, i.e., it increases with decreasing numerical aperture NA. In this case, we can assume that the field preserves the original polarization of the beams. However, with tight focusing, the influence of the type of polarization will be significant. We will show this using two examples with linear polarization, when the beam polarization is co-directional to the beam separation line, i.e., in our case, horizontally spaced beams are directed along the x -axis and perpendicular, i.e., directed along the y -axis.

Figure 2 shows the simulation results for two Gaussian beams horizontally displaced in the input plane relative to each other with the same linear x -polarization (Figure 2a) $[G(x - x_0, y) + G(x + x_0, y)]\mathbf{e}_x$, $x_0 = 80 \mu\text{m}$, $\mathbf{e}_x = (1, 0)^T$.

In this case, instead of Equation (12), we get:

$$\begin{aligned} E_x &= 2c_{x1} \cos \theta_0 \cos(\alpha x), \\ E_y &= 0, \\ E_z &= -2c_{x1}i \sin \theta_0 \sin(\alpha x). \end{aligned} \tag{14}$$

As follows from Equation (12), the y -component will be absent, and the x - and z -components will change in anti-phase (Figure 2b). Moreover, taking into account paraxiality, the intensity of the longitudinal component will be small, and an amplitude grating will be observed (Figure 2d). With sharp focusing, the influence of the longitudinal component increases, which leads to a decrease in grating contrast (Figure 2e). In both cases, the original polarization is completely preserved.

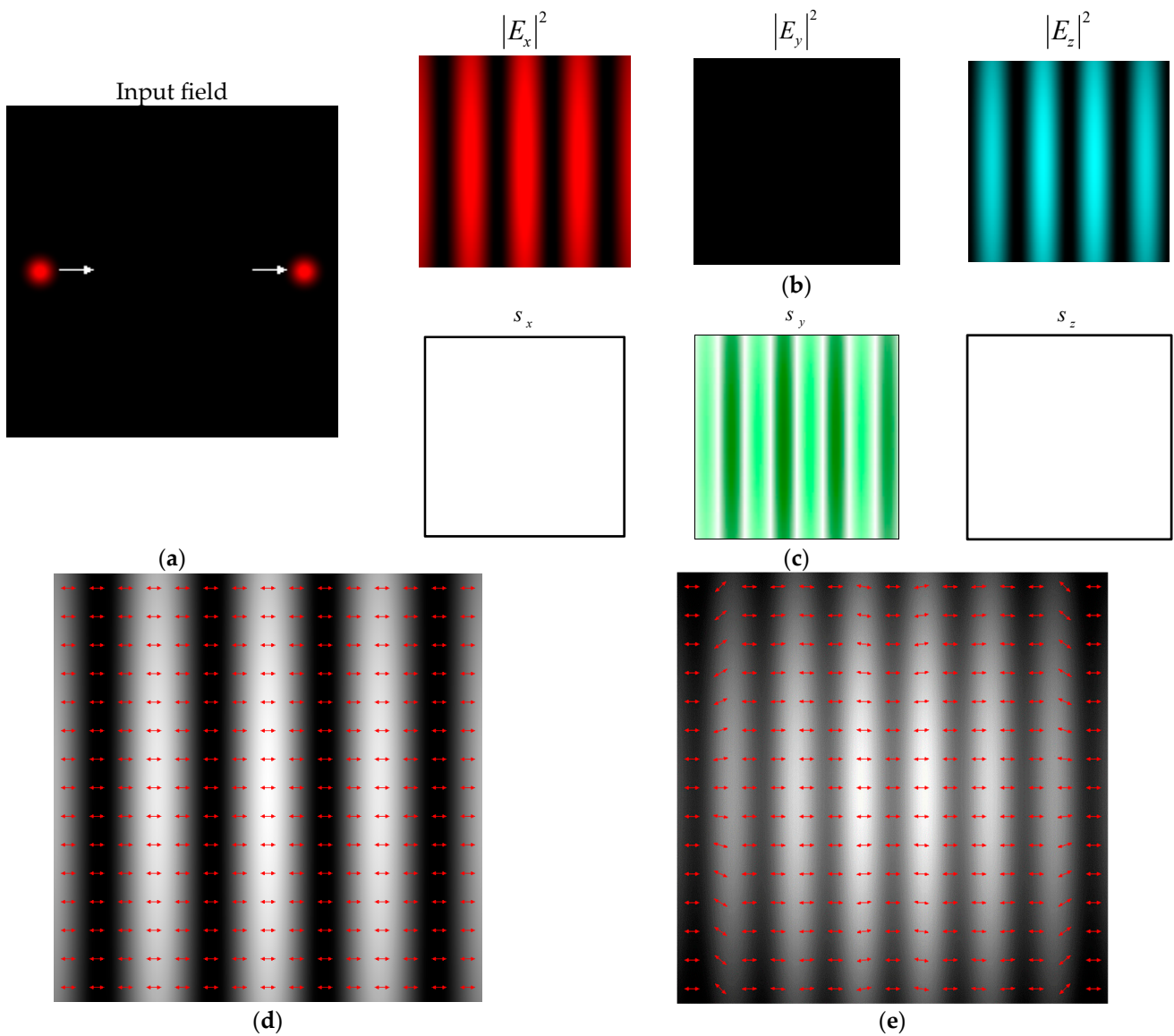


Figure 2. Simulation results for two Gaussian beams with the same linear x -polarization: (a) input field; (b) intensity distributions of the x -, y -, and z -components of the electric field; and (c) distributions of the x -, y -, and z -components of the SAM density, as well as the pattern of the total intensity with the state of polarization (shown by arrows) in (d) the paraxial case and (e) in the case of sharp focusing.

The SAM density distribution components in Equation (10) have the following form:

$$\begin{aligned}
 s_x &= 0, \\
 s_y &= 2 \sin(2\theta_0) \sin(2\alpha x), \\
 s_z &= 0.
 \end{aligned}
 \tag{15}$$

Thus, only the transverse y -component of the SAM is non-zero (Figure 2c), the distribution of which corresponds to a vertical grating with twice the frequency compared to the electric field components in Equation (14) (compare to Figure 2b,c). In this case, the rotation of the particles around its axis in the direction of the light propagation is expected. Moreover, in adjacent lines of different levels (corresponding to positive and negative values), rotation will occur in opposite directions.

Figure 3 shows similar simulation results for two Gaussian beams with the same linear y -polarization (Figure 3a) $[G(x - x_0, y) + G(x + x_0, y)]\mathbf{e}_y$, $x_0 = 80 \mu\text{m}$, $\mathbf{e}_y = (0, 1)^T$.

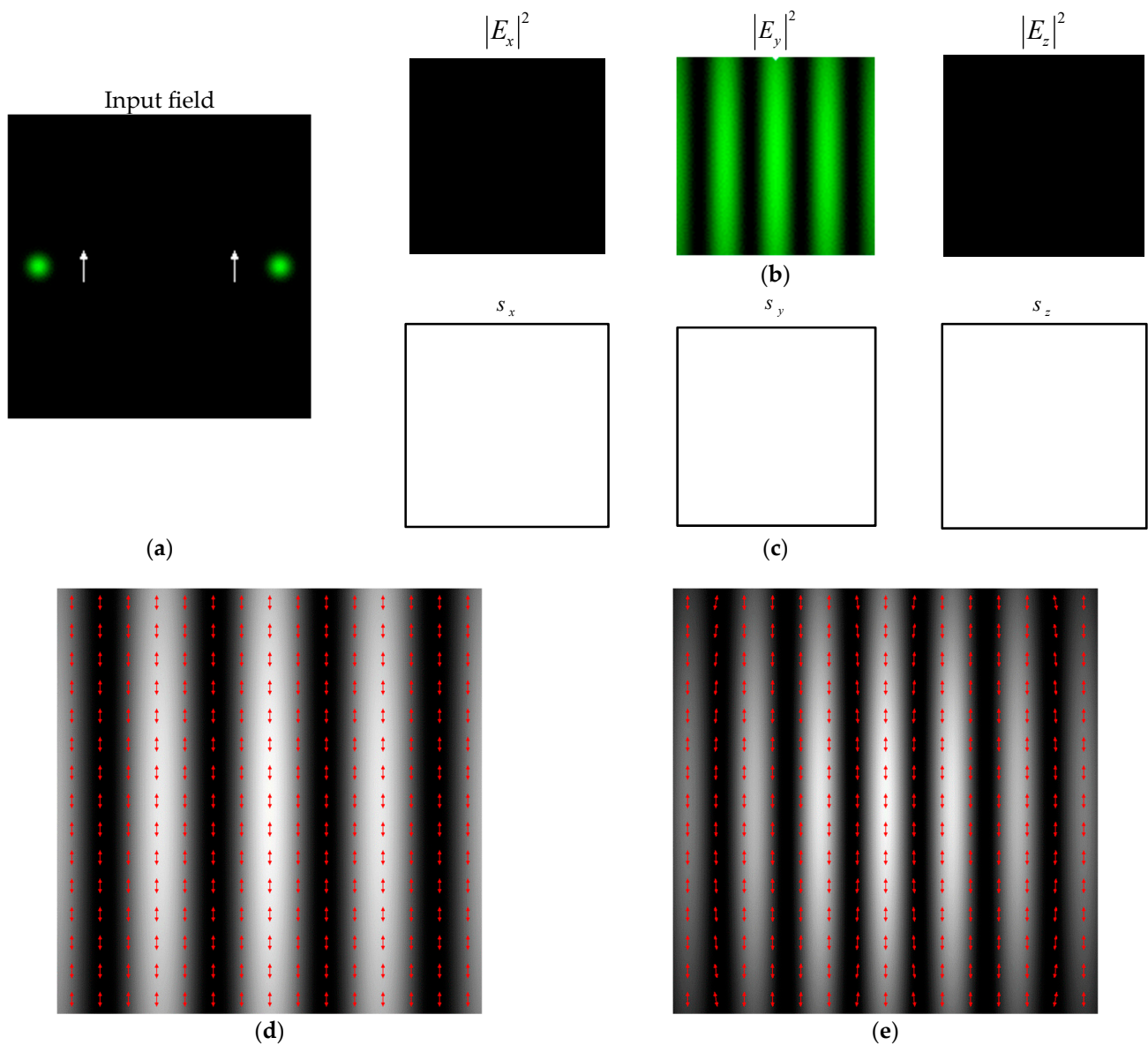


Figure 3. (a–e) Simulation results for two Gaussian beams with the same linear y -polarization (the rest is as in Figure 2).

In this case, instead of Equation (12), we get:

$$\begin{aligned} E_x &= 0, \\ E_y &= 2c_{y1} \cos(\alpha x), \\ E_z &= 0. \end{aligned} \tag{16}$$

Expression (16) actually corresponds to a scalar field, which only has a non-zero y -component (Figure 3b). This case is special in that the contrast of the amplitude grating does not change at any numerical aperture; only the grating period changes (Figure 3d,e). The fact of high contrast of the interference grating in this case was noted in [59,60] and was used for laser processing of polarization-sensitive materials.

It is interesting to note that all components of the SAM density distribution in this case are equal to zero:

$$\begin{aligned} s_x &= 0, \\ s_y &= 0, \\ s_z &= 0. \end{aligned} \tag{17}$$

Thus, the field does not even have local areas with non-zero SAM (Figure 3c).

3.1.2. Two Beams with Orthogonal Linear Polarization: $\mathbf{c}_1 = \begin{bmatrix} 1 \\ 0 \end{bmatrix}, \mathbf{c}_2 = \begin{bmatrix} 0 \\ 1 \end{bmatrix}$

In this example, orthogonal linear polarizations are considered (Figure 4a). Here, no transformation according to Euler’s formulas occurs, but one of the terms of each component in Equation (9) becomes zero:

$$\begin{aligned} E_x &= \cos \theta_0 \exp(i\alpha x), \\ E_y &= \exp(-i\alpha x), \\ E_z &= -\sin \theta_0 \exp(i\alpha x). \end{aligned} \tag{18}$$

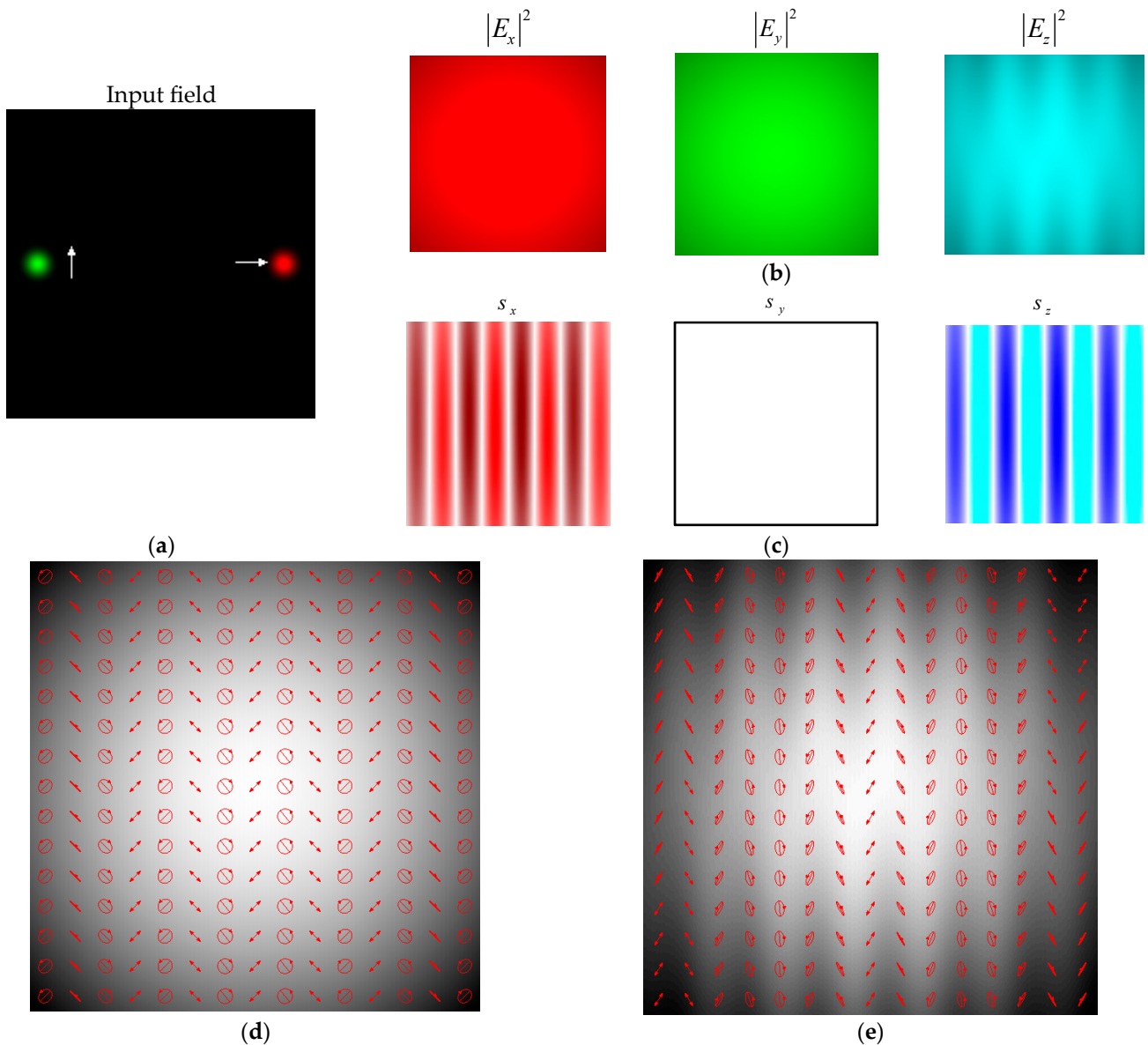


Figure 4. (a–e) Simulation results for two Gaussian beams with orthogonal linear polarization (the rest is as in Figure 2).

The intensity of each component is *independent of x* (Figure 4b), as well as the total intensity. In this case, the amplitude grating is not formed at any numerical aperture, but the polarization state becomes inhomogeneous and changes along with the x-coordinate (Figure 4d,e). Thus, a purely polarization grating is formed, which can also be used to form

a relief in polarization-sensitive films [25,42]. This is a significant difference from example of Section 3.1.1.

The SAM density distribution components are the following:

$$\begin{aligned} s_x &= -2 \sin \theta_0 \sin(2\alpha x), \\ s_y &= 0, \\ s_z &= -2 \cos \theta_0 \sin(2\alpha x). \end{aligned} \tag{19}$$

In this case, the spatial distribution in the transverse x -component and in the longitudinal component is the same (Figure 4c). Thus, the trapped particles will exhibit complex rotation in both the transverse and longitudinal directions. Moreover, the values in the longitudinal component with increasing numerical aperture (with sharp focusing) will decrease compared to the values in the transverse component, i.e., the particles will predominantly rotate in the direction of beam propagation.

3.1.3. Two Beams with Orthogonal Circular Polarizations: $\mathbf{c}_1 = \frac{1}{\sqrt{2}} \begin{bmatrix} 1 \\ i \end{bmatrix}, \mathbf{c}_2 = \frac{1}{\sqrt{2}} \begin{bmatrix} 1 \\ -i \end{bmatrix}$

In the case of interference of two beams with opposite circular polarizations (Figure 5a), we obtain:

$$\begin{aligned} E_x &= \sqrt{2} \cos \theta_0 \cos(\alpha x), \\ E_y &= -\sqrt{2} \sin(\alpha x), \\ E_z &= -\sqrt{2}i \sin \theta_0 \sin(\alpha x). \end{aligned} \tag{20}$$

Here, a transformation of polarization took place: It became *linear*. Moreover, the direction of polarization changes periodically in accordance with parameter α (Figure 5d,e). This fact was noted earlier in [19,23] and was used for laser patterning of polarization-sensitive materials [42,59–61].

Note, in the paraxial case, that the overall intensity is close to a uniform distribution (Figure 5d). This occurs due to the addition of the intensities of the transverse components varying in anti-phase. The work [59] also noted a rather low contrast of the gratings formed in this case compared to the interference of y -polarized beams. However, with tight focusing, a grating relief will appear (Figure 5e) as the energy from the x -component is redistributed to the longitudinal component, enhancing the y -component. In this way, both a polarization and an amplitude grating will be formed. This fact ensures effective writing of diffraction gratings on the surface of chalcogenide glasses [60].

The SAM density distribution components are the following:

$$\begin{aligned} s_x &= 4 \sin \theta_0 \sin^2(\alpha x), \\ s_y &= \sin(2\theta_0) \sin(2\alpha x), \\ s_z &= 0. \end{aligned} \tag{21}$$

In this case, the longitudinal component contains only zero values, and the transverse x -component contains only positive values (Figure 5c).

Similar results are observed during the interference of two beams with orthogonal diagonal linear polarizations [60]. However, the state of polarization in this case will be similar to the version considered in Section 3.1.2, which will also lead to the formation of a non-uniform distribution of the SAM density.

3.2. Superposition of Four Beams Spaced Horizontally and Vertically

The analytical results discussed in the previous section can be quite simply generalized to the case of four beams spaced horizontally and vertically. In this case, $\phi_1 = 0^\circ, \phi_2 = 90^\circ, \phi_3 = 180^\circ, \text{ and } \phi_4 = 270^\circ$. If we substitute these values into Equations (7) and (8), we get:

$$\begin{aligned} E_x &= \cos \theta_0 [c_{x1} \exp(i\alpha x) + c_{x3} \exp(-i\alpha x)] + [c_{x2} \exp(i\alpha y) + c_{x4} \exp(-i\alpha y)], \\ E_y &= [c_{y1} \exp(i\alpha x) + c_{y3} \exp(-i\alpha x)] + \cos \theta_0 [c_{y2} \exp(i\alpha y) + c_{y4} \exp(-i\alpha y)], \\ E_z &= -\sin \theta_0 \{ [c_{x1} \exp(i\alpha x) - c_{x3} \exp(-i\alpha x)] + [c_{y2} \exp(i\alpha y) - c_{y4} \exp(-i\alpha y)] \}. \end{aligned} \tag{22}$$

First, we shall look at two examples where the polarization of all four beams is the same. In one case it is linear, and in the other it is circular.

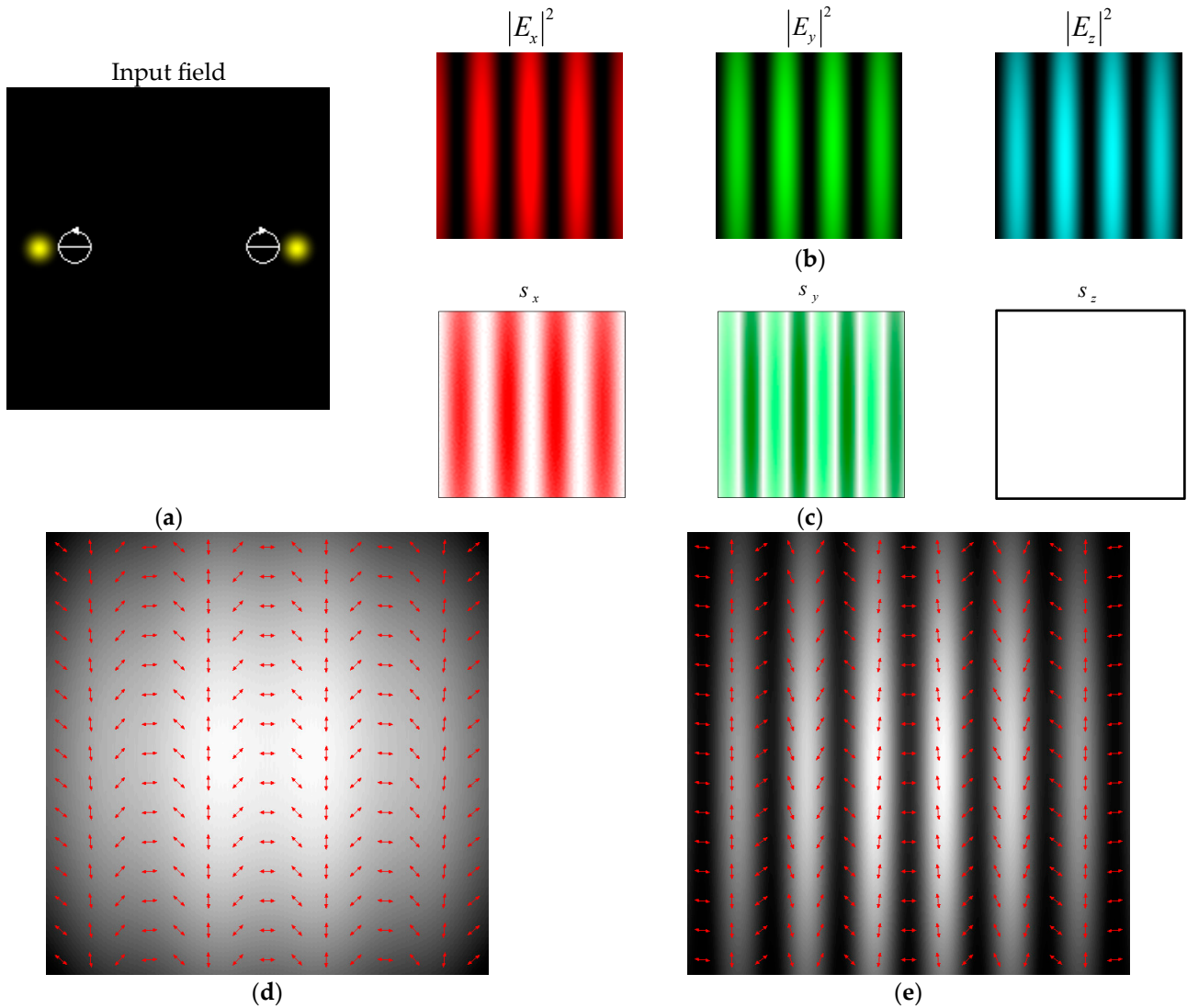


Figure 5. (a–e) Simulation results for two Gaussian beams with opposite circular polarizations (the rest is as in Figure 2).

3.2.1. Four Beams with the Same Linear X-Polarization: $\mathbf{c}_p = \begin{bmatrix} 1 \\ 0 \end{bmatrix}$

This case is the simplest (Figure 6a):

$$\begin{aligned} E_x &= 2[\cos \theta_0 \cos(\alpha x) + \cos(\alpha y)], \\ E_y &= 0, \\ E_z &= -2i \sin \theta_0 \sin(\alpha x). \end{aligned} \tag{23}$$

From Expression (23), it follows that the polarization remained *linear* (Figure 6d,e), although the field structure has changed compared to example of Section 3.1.1.

The intensity of the x-component is a two-dimensional grating, the y-component is absent, and the intensity of the longitudinal component depends only on the x coordinate, i.e., it corresponds to a one-dimensional grating (Figure 6b).

In the paraxial case, a regular-amplitude two-dimensional grating will be observed, corresponding to the distribution of the x-component (Figure 6d). With tight focusing, the

contribution of the longitudinal component will increase, which will lead to the elongation of the light spots of the grating along the direction of field polarization (Figure 6e).

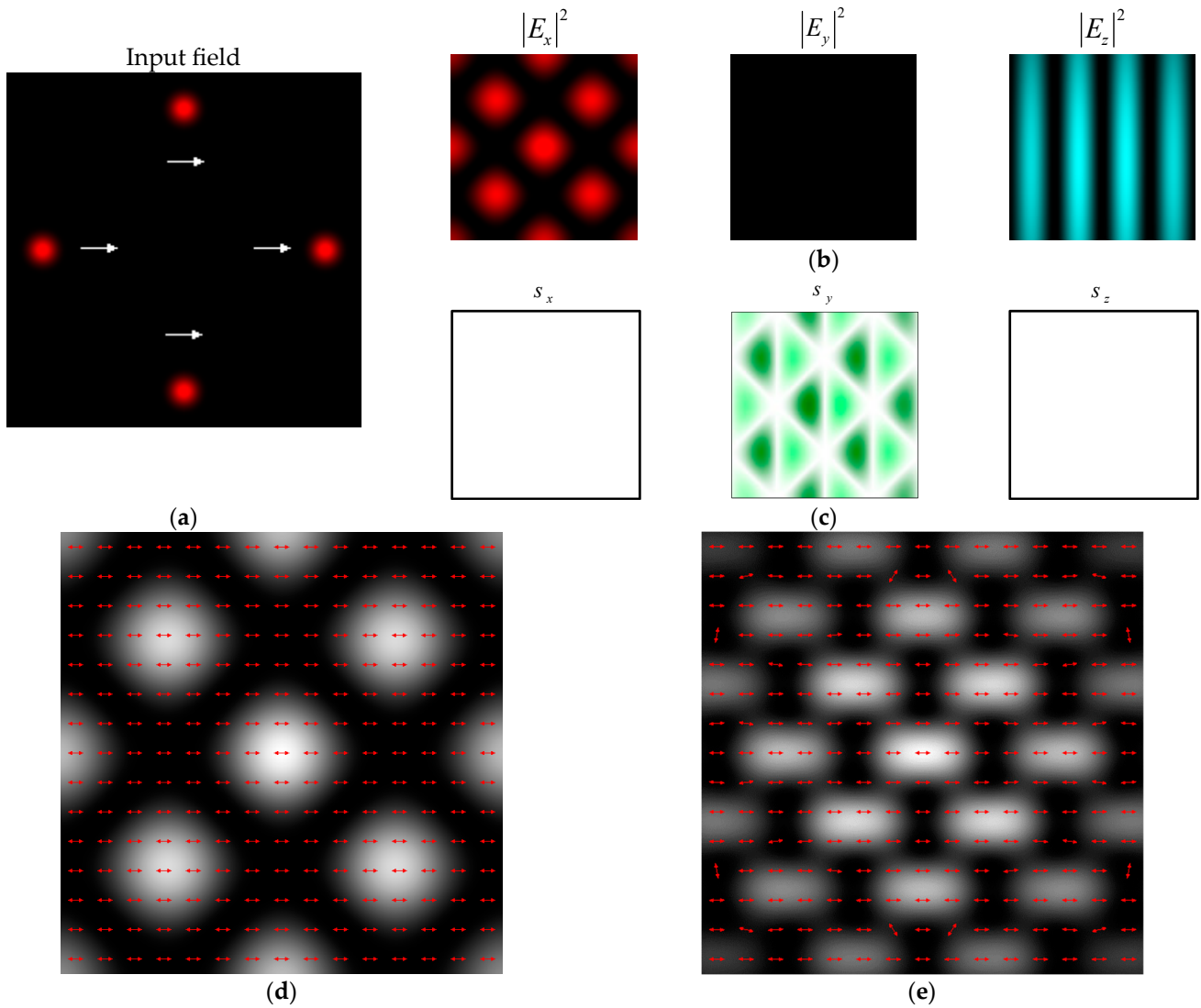


Figure 6. (a–e) Simulation results for four Gaussian beams with the same linear x-polarizations (the rest as in Figure 2).

The SAM density distribution has only a non-zero y -component:

$$\begin{aligned} s_x &= 0, \\ s_y &= 8 \sin \theta_0 \sin(\alpha x) [\cos \theta_0 \cos(\alpha x) + \cos(\alpha y)], \\ s_z &= 0. \end{aligned} \tag{24}$$

This component appears as a two-dimensional lattice with triangular regions of positive and negative values (Figure 6c) in which trapped particles will rotate in opposite directions. As the numerical aperture increases (with tight focusing), the SAM values will increase, but the grating period will decrease, and the size of the areas will also decrease. Therefore, a clear rotational movement can only be observed in small particles (the size of which corresponds to the size of individual regions).

Note that for linear x -polarization, the result will be approximately the same if the directions at various points are reversed. In this case, only a displacement of the formed structure can occur.

3.2.2. Four Beams with the Same Circular Polarizations: $\mathbf{c}_p = \frac{1}{\sqrt{2}} \begin{bmatrix} 1 \\ i \end{bmatrix}$

This case is more interesting (Figure 7a):

$$\begin{aligned} E_x &= \sqrt{2}[\cos \theta_0 \cos(\alpha x) + \cos(\alpha y)], \\ E_y &= \sqrt{2}i[\cos(\alpha x) + \cos \theta_0 \cos(\alpha y)], \\ E_z &= -\sqrt{2}i \sin \theta_0 [\sin(\alpha x) + i \sin(\alpha y)]. \end{aligned} \tag{25}$$

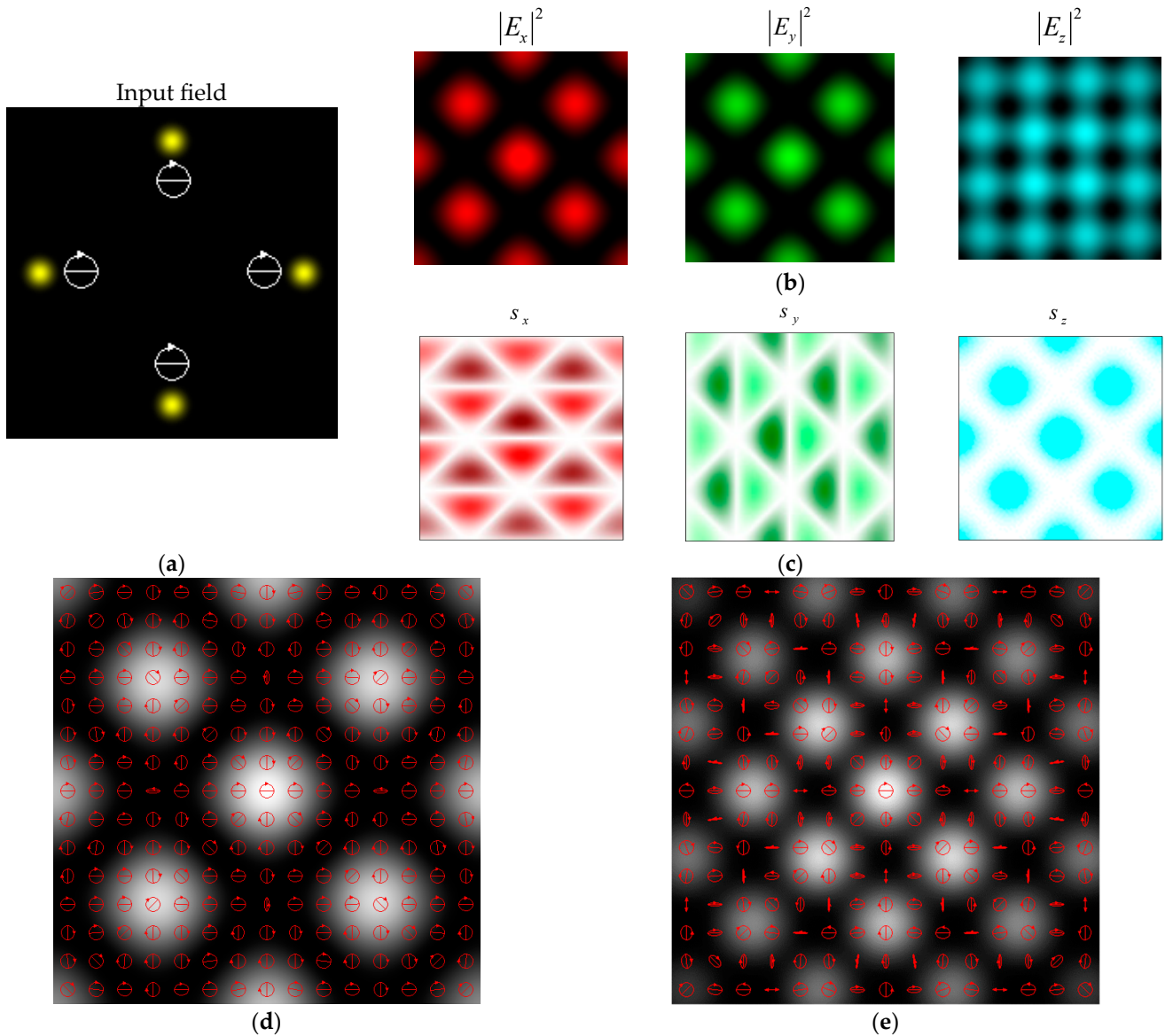


Figure 7. (a–e) Simulation results for four Gaussian beams with identical circular polarizations (the rest is as in Figure 2).

As follows from Expression (25), in the paraxial approximation ($\cos \theta_0 \approx 1$) the polarization remains virtually circular (Figure 7d), but with sharp focusing ($\cos \theta_0 \approx 0$). Instead of circular, it becomes elliptical (Figure 7e). Note that the longitudinal component has a two-dimensional periodic set of points with a vortex singular phase.

Although the intensity of each of the transverse components in Expression (25) is asymmetric with respect to the permutation of x and y , their sum will be symmetric:

$$|E_x|^2 + |E_y|^2 = 2 \left\{ \left(1 + \cos^2 \theta_0 \right) \left[\cos^2(\alpha x) + \cos^2(\alpha y) \right] + 4 \cos \theta_0 \cos(\alpha x) \cos(\alpha y) \right\}. \tag{26}$$

The amplitudes of the transverse components are *not* equal, but the phase difference is always $\pm 90^\circ$. Therefore, the axes of the polarization ellipses are located either horizontally or vertically (Figure 7e). *Circular* polarization is preserved only on lines where $\cos^2(\alpha y) = \cos^2(\alpha x)$.

All components of the SAM density distribution are non-zero:

$$\begin{aligned} s_x &= -4 \sin \theta_0 \sin(\alpha y) [\cos(\alpha x) + \cos \theta_0 \cos(\alpha y)], \\ s_y &= 4 \sin \theta_0 \sin(\alpha x) [\cos \theta_0 \cos(\alpha x) + \cos(\alpha y)], \\ s_z &= 4 [\cos \theta_0 \cos(\alpha x) + \cos(\alpha y)] [\cos(\alpha x) + \cos \theta_0 \cos(\alpha y)]. \end{aligned} \tag{27}$$

The form of the transverse components in Expression (27) represents two-dimensional lattices with triangular regions having positive and negative values. Note that the longitudinal component, which is responsible for the rotation of trapped particles in the transverse plane, in the paraxial approximation will have mostly positive values (the area of regions with negative values is small, and the negative values themselves are close to zero) (Figure 7a). This corresponds to rotation only in one direction (in the same direction as the original polarization). At sharp focusing ($\cos \theta_0 \approx 0$), areas with negative values will be more visible.

Next, we shall consider examples in which a certain symmetry or some features occur.

3.2.3. Radial-Type Distribution: $\mathbf{c}_1 = \begin{bmatrix} 1 \\ 0 \end{bmatrix}, \mathbf{c}_2 = \begin{bmatrix} 0 \\ 1 \end{bmatrix}, \mathbf{c}_3 = \begin{bmatrix} -1 \\ 0 \end{bmatrix}, \mathbf{c}_4 = \begin{bmatrix} 0 \\ -1 \end{bmatrix}$

This variant corresponds to the simulation of *radial* polarization (Figure 8a):

$$\begin{aligned} E_x &= 2i \cos \theta_0 \sin(\alpha x), \\ E_y &= 2i \cos \theta_0 \sin(\alpha y), \\ E_z &= -2 \sin \theta_0 [\cos(\alpha x) + \cos(\alpha y)]. \end{aligned} \tag{28}$$

As can be seen from Expression (28), the transverse components correspond to one-dimensional lattices in orthogonal directions, and the longitudinal component corresponds to a two-dimensional grating (Figure 8b). The polarization is non-uniform linear (Figure 8d,e), and the inclination angle of the polarization vectors is determined by the relations $\cos \beta = \sin(\alpha x)$ and $\sin \beta = \sin(\alpha y)$. Note that the structure of the total intensity changes when the numerical aperture of the focusing system changes due to the contribution of the longitudinal component (Figure 8d,e).

The components of the SAM density distribution are defined as follows:

$$\begin{aligned} s_x &= 4 \sin(2\theta_0) \sin(\alpha y) [\cos(\alpha x) + \cos(\alpha y)], \\ s_y &= -4 \sin(2\theta_0) \sin(\alpha x) [\cos(\alpha x) + \cos(\alpha y)], \\ s_z &= 0. \end{aligned} \tag{29}$$

The transverse components in Expression (29) are two-dimensional gratings with triangular regions having positive and negative values, and there are no non-zero values in the longitudinal component (Figure 8c).

3.2.4. Azimuthal-Type Distribution: $\mathbf{c}_1 = \begin{bmatrix} 0 \\ -1 \end{bmatrix}, \mathbf{c}_2 = \begin{bmatrix} 1 \\ 0 \end{bmatrix}, \mathbf{c}_3 = \begin{bmatrix} 0 \\ 1 \end{bmatrix}, \mathbf{c}_4 = \begin{bmatrix} -1 \\ 0 \end{bmatrix}$

This variant corresponds to the *azimuthal* polarization simulation (Figure 9a):

$$\begin{aligned} E_x &= 2i \sin(\alpha y), \\ E_y &= -2i \sin(\alpha x), \\ E_z &= 0. \end{aligned} \tag{30}$$

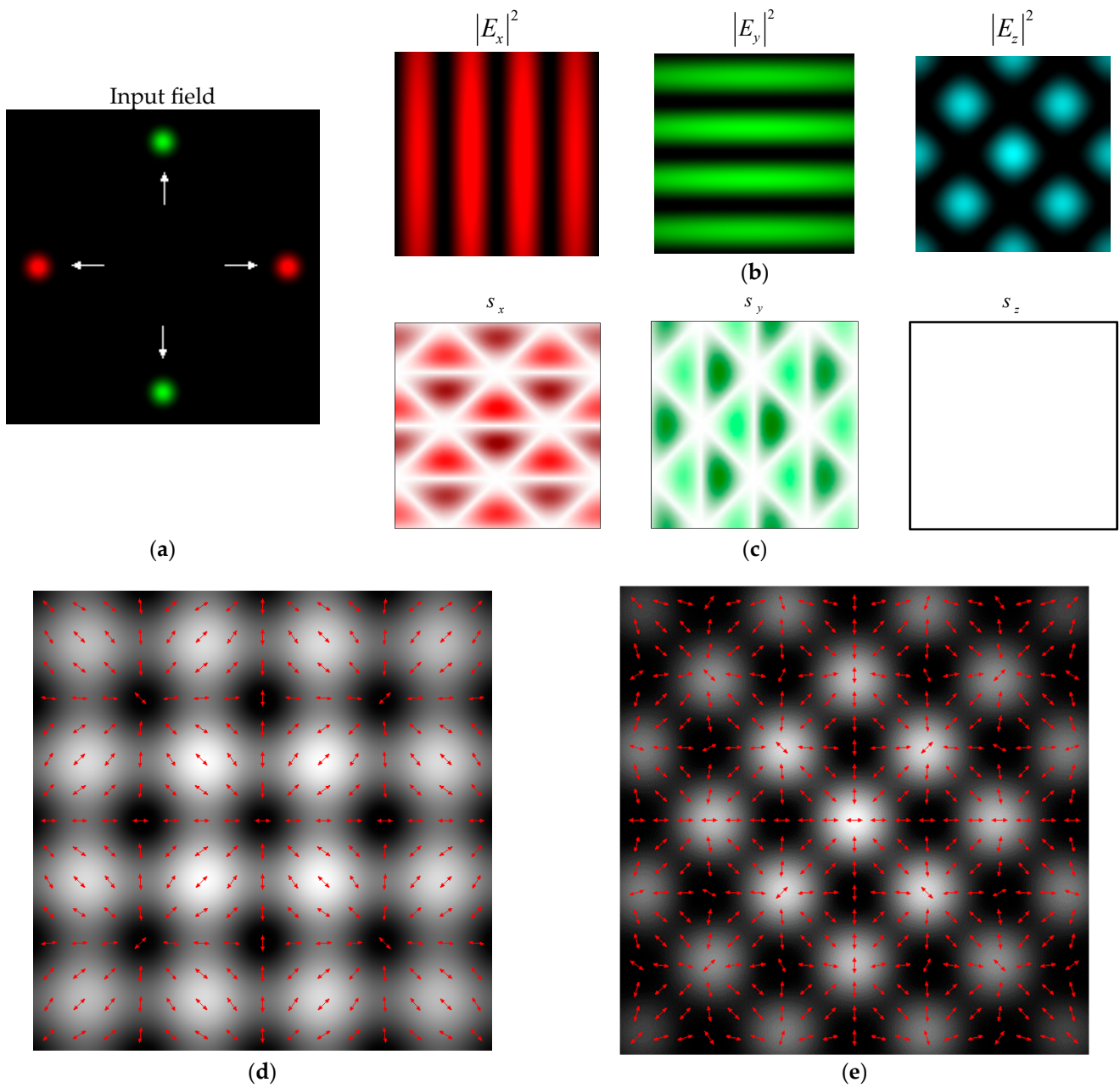


Figure 8. (a–e) Simulation results for four Gaussian beams with orthogonal linear polarizations of the radial type (the rest of the description is as in Figure 2).

As can be seen, there is *no longitudinal* component. In the transverse components, compared to Expression (20), there is no $\cos\theta_0$ multiplier, the sines have swapped places, and a minus sign has appeared in the x -component (Figure 9b). The absence of the $\cos\theta_0$ multiplier in this case ensures the invariance (up to scale) of the structure of the total intensity when changing the numerical aperture of the focusing system (Figure 9d,e). This is one of the differences from the previous case 3.2.3 of radial arrangement. The polarization is non-uniform *linear* (Figure 9d,e), and the angle of inclination of the polarization vectors is found from the equalities $\cos \beta = \sin(\alpha y)$ and $\sin \beta = -\sin(\alpha x)$.

All components of the SAM density distribution are equal to zero in this case (Figure 9c):

$$\begin{aligned} s_x &= 0, \\ s_y &= 0, \\ s_z &= 0. \end{aligned} \tag{31}$$

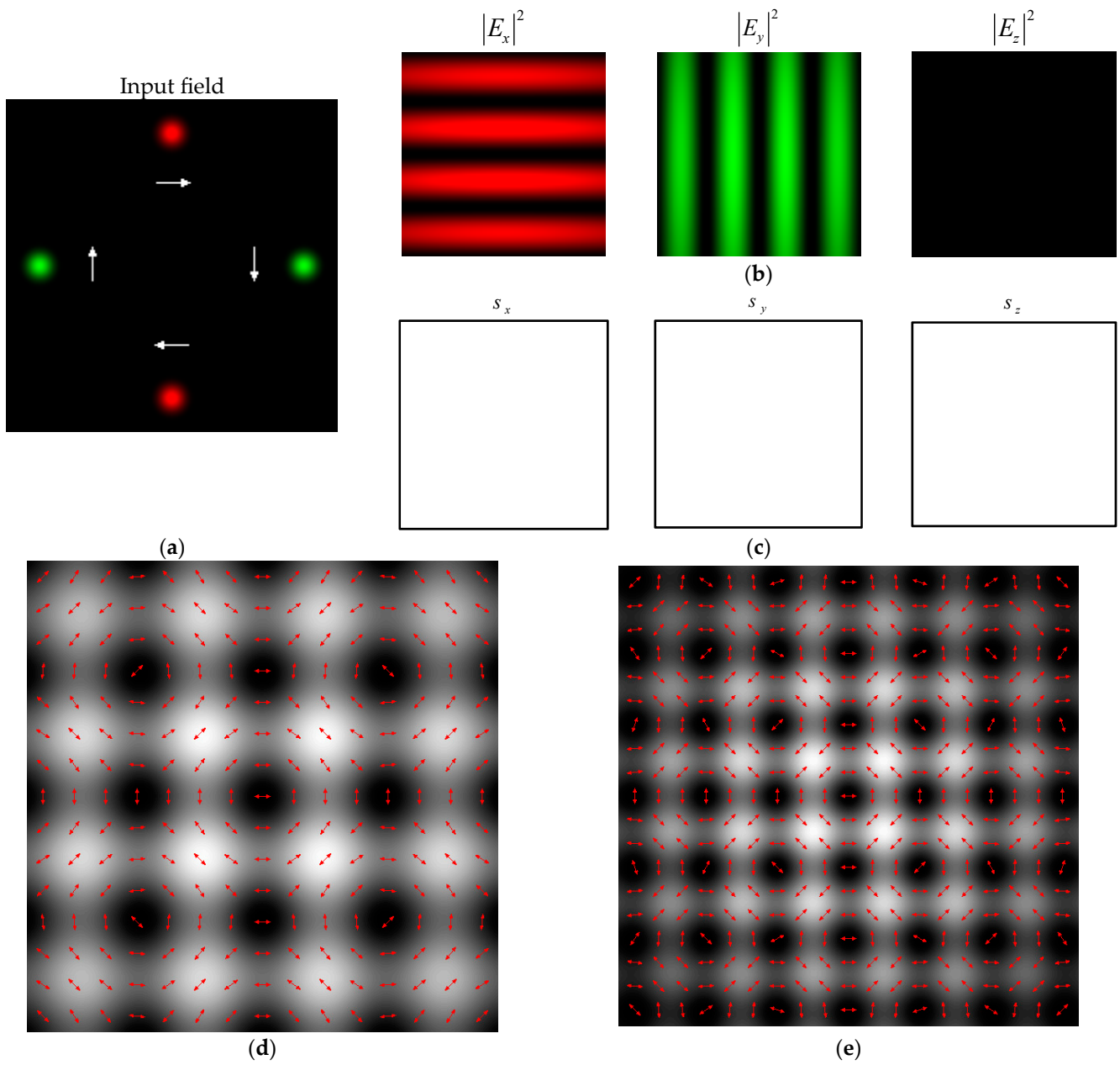


Figure 9. (a–e) Simulation results for four Gaussian beams with orthogonal linear polarizations of azimuthal type (the rest of the description is as in Figure 2).

3.2.5. Mixed Radial–Azimuthal Distribution:

$$\mathbf{c}_1 = \frac{1}{\sqrt{2}} \begin{bmatrix} 1 \\ -1 \end{bmatrix}, \mathbf{c}_2 = \frac{1}{\sqrt{2}} \begin{bmatrix} 1 \\ 1 \end{bmatrix}, \mathbf{c}_3 = \frac{1}{\sqrt{2}} \begin{bmatrix} -1 \\ 1 \end{bmatrix}, \mathbf{c}_4 = \frac{1}{\sqrt{2}} \begin{bmatrix} -1 \\ -1 \end{bmatrix}$$

This variant corresponds to a mixed radial–azimuthal distribution [32,62,63] of polarization (Figure 10a) with the following distribution of electric field components:

$$\begin{aligned} E_x &= \sqrt{2}i[\cos \theta_0 \sin(\alpha x) + \sin(\alpha y)], \\ E_y &= \sqrt{2}i[\cos \theta_0 \sin(\alpha y) - \sin(\alpha x)], \\ E_z &= -\sqrt{2} \sin \theta_0 [\cos(\alpha x) + \cos(\alpha y)]. \end{aligned} \tag{32}$$

The longitudinal component is the same as in Section 3.2.3. In the paraxial case, the maxima of the x -component lie on straight lines with a slope close to 45 degrees, and the maxima of the y -component lie on straight lines with a slope close to 135 degrees

(Figure 10b). The distribution of the longitudinal component has two axes of symmetry. The polarization is non-uniform *linear* (Figure 10d,e), and the angle of inclination of the polarization vectors is found from the equalities $\cos \beta = \cos(\theta_0)\sin(\alpha x) + \sin(\alpha y)$ and $\sin \beta = \cos(\theta_0)\sin(\alpha y) - \sin(\alpha x)$.

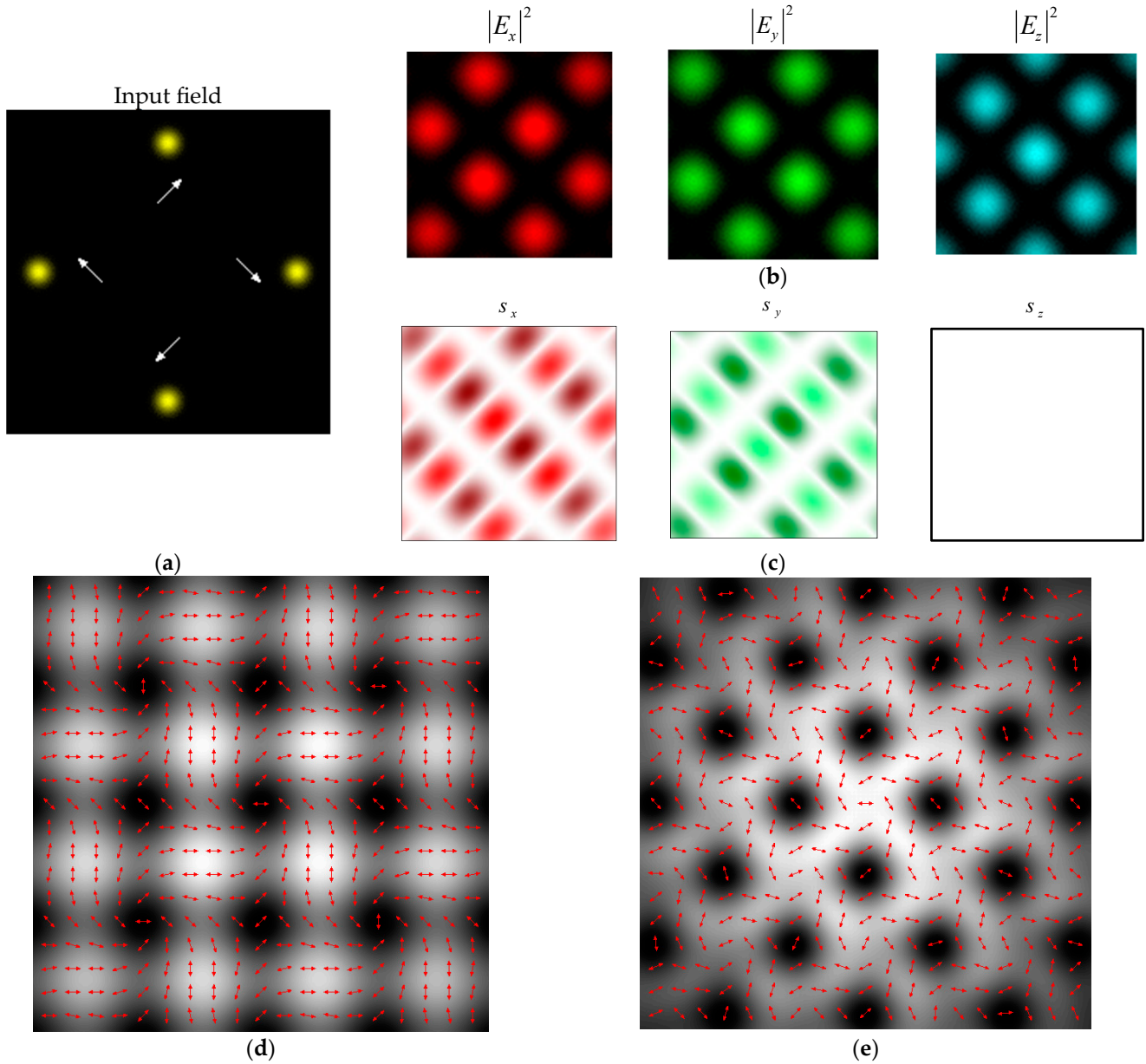


Figure 10. (a–e) Simulation results for four Gaussian beams with linear polarizations of the spiral type (the rest of the description is as in Figure 2).

The components of the SAM density distribution are defined as follows (Figure 10c):

$$\begin{aligned}
 s_x &= 4 \sin \theta_0 [\cos \theta_0 \sin(\alpha y) - \sin(\alpha x)] [\cos(\alpha x) + \cos(\alpha y)], \\
 s_y &= -4 \sin \theta_0 [\cos \theta_0 \sin(\alpha x) + \sin(\alpha y)] [\cos(\alpha x) + \cos(\alpha y)], \\
 s_z &= 0.
 \end{aligned}
 \tag{33}$$

The form of the transverse components in Expression (33) are two-dimensional gratings with areas of positive and negative values shaped like rounded rectangles. The longitudinal component is zero (Figure 10c).

3.2.6. Pairwise Orthogonal Circular Polarizations:

$$\mathbf{c}_1 = \mathbf{c}_2 = \frac{1}{\sqrt{2}} \begin{bmatrix} 1 \\ i \end{bmatrix}, \mathbf{c}_3 = \mathbf{c}_4 = \frac{1}{\sqrt{2}} \begin{bmatrix} 1 \\ -i \end{bmatrix}$$

In this section, we obtain the following electric field components (Figure 11b):

$$\begin{aligned} E_x &= \sqrt{2}[\cos \theta_0 \cos(\alpha x) + \cos(\alpha y)], \\ E_y &= -\sqrt{2}[\sin(\alpha x) + \cos \theta_0 \sin(\alpha y)], \\ E_z &= -i\sqrt{2} \sin \theta_0 [\sin(\alpha x) + \cos(\alpha y)]. \end{aligned} \tag{34}$$

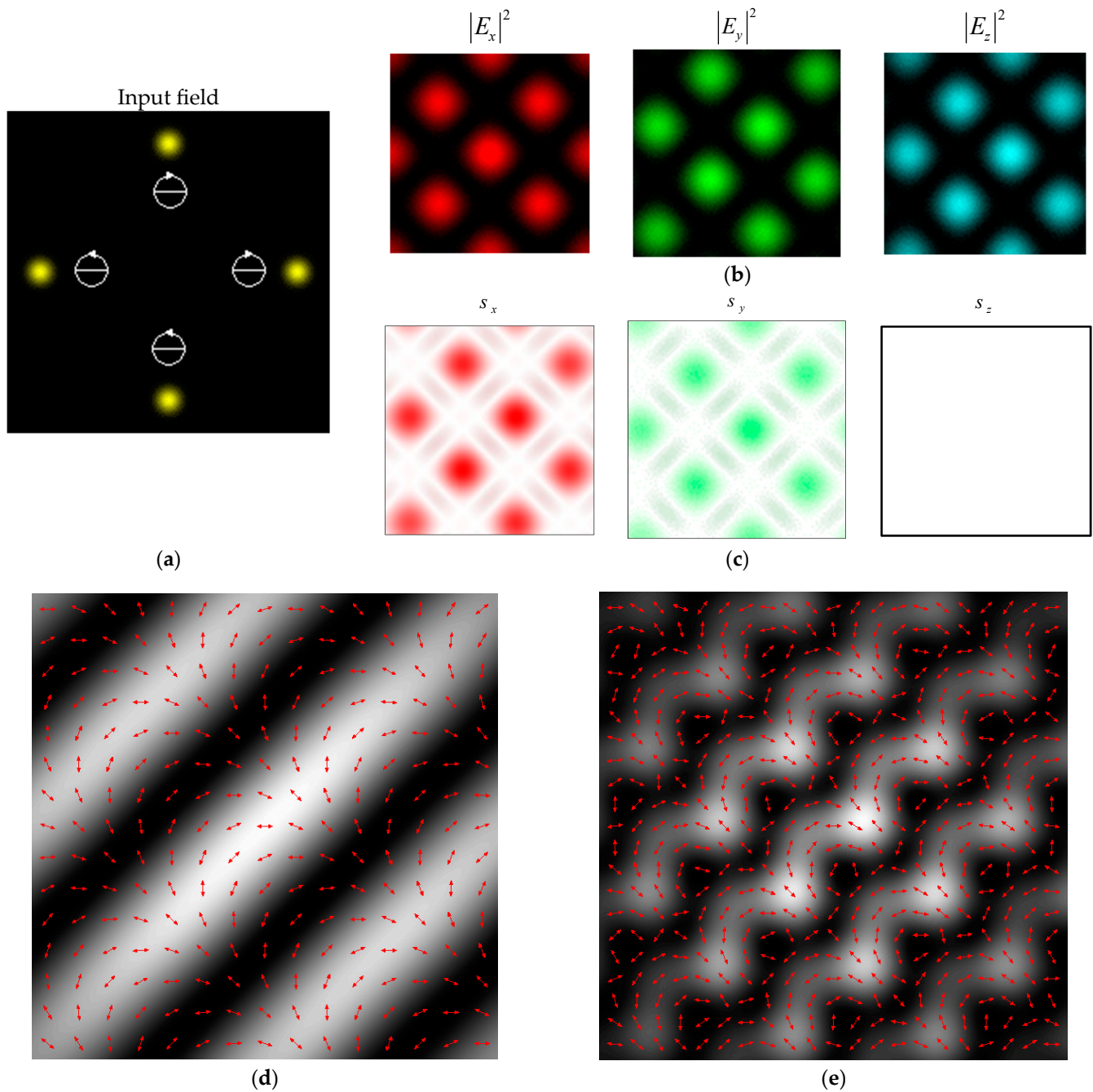


Figure 11. (a–e) Simulation results for four Gaussian beams with two pairs of orthogonal circular polarizations (the rest of the description is as in Figure 2).

It can be seen that the polarization of the formed field is non-uniform *linear* (Figure 11d,e). The intensities of the *x*- and *y*-components are symmetrical (the *x*-component

has a maximum in the center, and the y -component has a minimum in the center) relative to the origin, while the center of the z -component is shifted horizontally. The latter property appears in the total intensity pattern in the non-paraxial case (Figure 11e). The intensity of the sum of the transverse components is:

$$\left[\cos^2 \theta_0 \cos^2(\alpha x) + \sin^2(\alpha x) \right] + \left[\cos^2(\alpha y) + \cos^2 \theta_0 \sin^2(\alpha y) \right] + 2 \cos \theta_0 \cos(x - y). \quad (35)$$

In the paraxial case, Expression (35) is approximately one-dimensional, as can be seen in Figure 11d. With sharp focusing, the influence of the longitudinal component increases and the field structure becomes more complex (Figure 11e).

The components of the SAM density distribution are following (Figure 11c):

$$\begin{aligned} s_x &= 4 \sin \theta_0 [\sin(\alpha x) + \cos \theta_0 \sin(\alpha y)] [\sin(\alpha x) + \cos(\alpha y)], \\ s_y &= 4 \sin \theta_0 [\cos \theta_0 \cos(\alpha x) + \cos(\alpha y)] [\sin(\alpha x) + \cos(\alpha y)], \\ s_z &= 0. \end{aligned} \quad (36)$$

From these equalities, it can be concluded that positive component values occupy a larger area than negative ones. The longitudinal component is zero.

4. Experimental Results

The optical setup used for the experimental generation and study of multi-beam interference patterns is shown in Figure 12a. In the experiments, a linearly polarized laser beam with a wavelength of 532 nm from a continuous solid-state laser MGL-U-532-1B was expanded using a combination of a micro-objective MO1 ($3.7\times$, $NA = 0.11$) and a lens L1 ($f_1 = 100$ mm). The linear polarizer PT1 made it possible to increase the contrast of the linear polarization of the laser beam. Then, mirrors M1 and M2 directed the beam into the diffractive optical element (DOE), which is a one- or two-dimensional binary diffraction grating used for splitting the laser beam and shaping two or four identical laser beams. The angle of divergence of split beams after the DOE was 0.85 degrees. A technological process comprising lithography and plasma etching was utilized to manufacture the DOEs [11]. The amplitude mask (AM) and the polarizing element PT2 were utilized to spatially filter the laser beam and create the necessary combination of two or four laser beams with the desired polarization states. In the case of generating two-beam interference patterns, the amplitude mask was a black screen with two transparent holes for laser beams propagating in the direction of ± 1 diffraction orders. In the case of generating four-beam interference patterns, the amplitude mask was a black screen with four transparent holes for laser beams propagating in the direction of ± 1 diffraction orders along the Cartesian coordinates x and y . The diameter of the holes was 1 mm, and the distance between holes in the amplitude mask was 2.5 mm. Micro-objective MO2 ($20\times$, $NA = 0.4$) projected the generated light field onto the matrix of a polarization video camera ImagingSource DZK 33UX250 (PCAM). This video camera is widely used to generate distributions of Stokes parameters of incident laser beams and can be used to reconstruct the polarization distribution of the light fields under study. However, this video camera allows one to measure only the first three Stokes parameters (St_0 , St_1 , and St_2). To measure the fourth Stokes parameter (St_3) and restore the ellipticity of the formed polarization ellipses in each pixel, an additional quarter-wave plate was used (the plate is not shown in Figure 12a). The procedure for reconstructing polarization distributions using Stokes parameters is described in [9]. Examples of intensity distributions and reconstructed polarization distributions experimentally obtained using two- and four-beam interference are shown in Figures 13 and 14. The results obtained are in good agreement with the simulation results presented in Figures 2–6, 8 and 9.

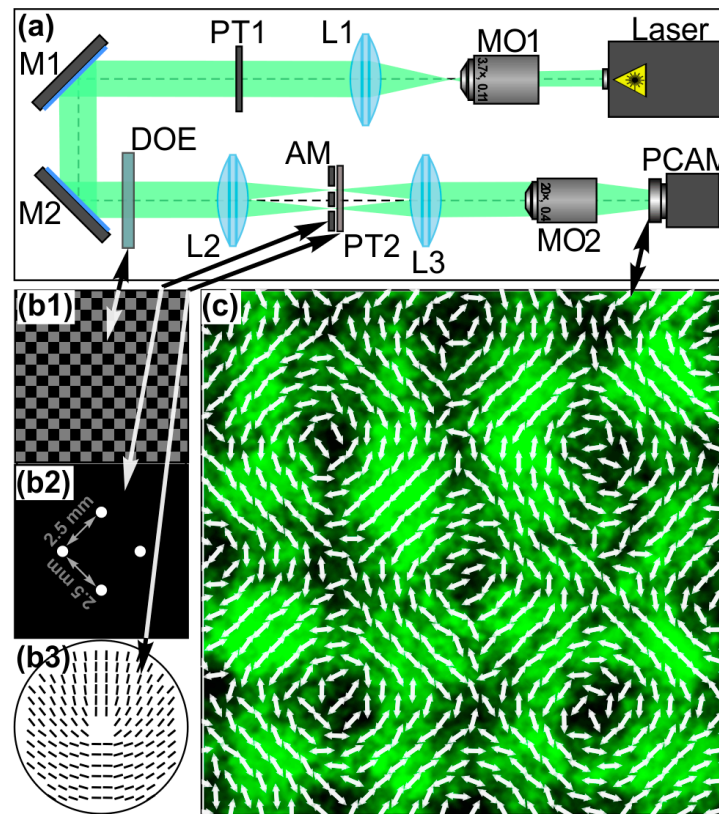


Figure 12. Experimental investigation of the generation of multi-beam interference patterns. (a) Optical setup: Laser is a cw solid-state laser MGL-U-532-1W; L1, L2, and L3 are spherical lenses ($f_1 = 100$ mm, $f_2 = 125$ mm, and $f_3 = 100$ mm); M1 and M2 are mirrors, PT1 is a linear polarizer, and DOE is a diffractive optical element in the form of a binary diffractive grating for the splitting of incident laser beams; AM is an amplitude mask, PT2 is a polarizing element, MO1 and MO2 are micro-objects (NA = 0.11 and 0.4), and PCAM is a ImagingSource DZK 33UX250 polarization video camera. (b1) Phase mask of the diffractive optical element (DOE) utilized to split an incident laser beam into four laser beams. (b2) Amplitude mask used for spatial filtering of the light field formed by the DOE. (b3) Local optical axis orientation of an S-waveplate utilized in the experiments for transformation of the polarization distribution of the incident light field. (c) Example of light field distributions (intensity and polarization vectors) of the experimentally generated light field corresponding to the modeling results presented in Figure 9.

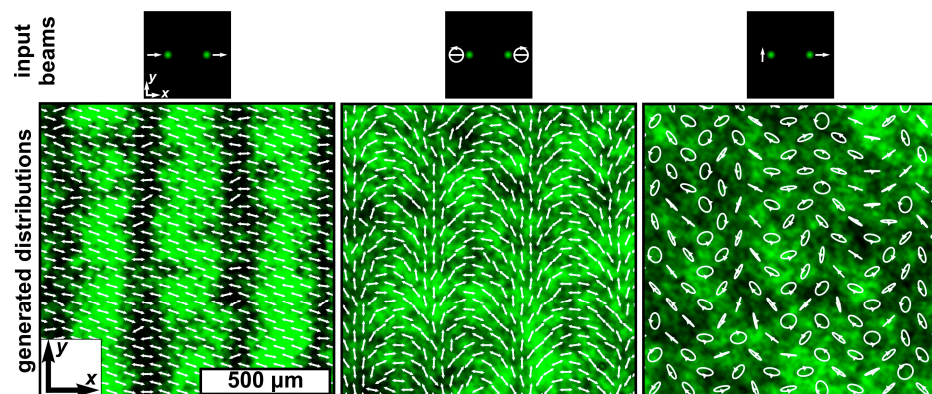


Figure 13. Intensity and polarization distributions of the experimentally generated two-beam interference patterns. White arrows and ellipses represent linear polarization vectors and polarization ellipses.

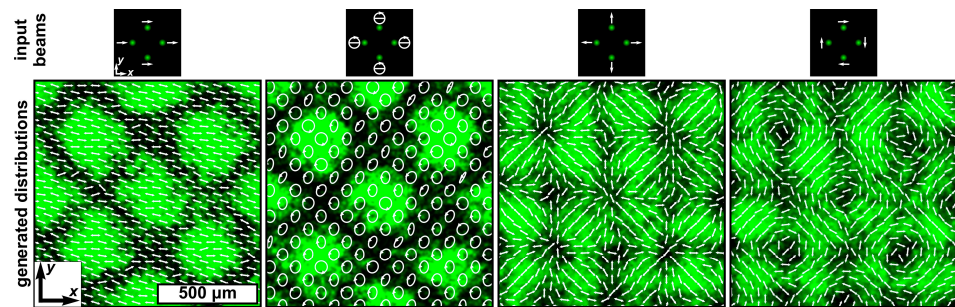


Figure 14. Intensity and polarization distributions of the experimentally generated four-beam interference patterns. White arrows and ellipses represent linear polarization vectors and polarization ellipses.

5. Discussion

A detailed theoretical and numerical analysis of the interference of two light beams with different polarization states allows us to more clearly understand the mechanism of formation of contrast amplitude gratings and purely polarization gratings.

It has been shown that the amplitude grating with the best contrast, which is independent of focusing sharpness, is achieved with linear polarization directed perpendicular to the line connecting the coplanar radiation sources (Figure 3a). The fact of high contrast of the interference grating in this case was noted in [59,60] and was used for laser processing of polarization-sensitive materials.

Purely polarization gratings (without amplitude changes) are formed in orthogonal states of polarization of coplanar beams—for example, with x- and y-polarization (Figure 4a) or circular polarizations of opposite directions (Figure 5a). In the formed field, the polarization state changes periodically; thus, a purely polarization grating is formed, which can also be used to form a relief in polarization-sensitive films [25,42,59–61].

The interference of four light beams with different polarization states allows a periodic light field to be formed whose polarization distribution is actually a set of polarization singularities corresponding to radially and azimuthally polarized beams (Figures 8 and 9). Such structures can expand the capabilities of the laser processing and structuring of materials, as well as the capture and manipulation of microparticles.

6. Conclusions

In this work, light fields formed as a result of the interference of two and four light beams with identical and different polarization states are numerically studied. Both linearly and circularly polarized beams are considered. The possibility of forming periodic light fields, the polarization distribution of which is actually a set of polarization singularities corresponding to radially and azimuthally polarized beams, is shown. For this purpose, combinations of four beams equidistant from the optical axis with a changing orientation of linear polarization, simulating a change in the polarization vector in a single radially or azimuthally polarized beam, were considered. In practice, such combinations can be formed using combinations of beam splitter cubes and half-wave plates or polarizing films. This approach, compared to the method of using sector polarizing plates, not only makes it possible to form periodically repeating sets of the required polarization singularities but also provides better quality of formation. In addition, the interference approach is known to potentially produce light spots with subwavelength resolution without the use of additional high-aperture focusing optics. However, for this, it is necessary to increase the values of the convergence angles of the interfering beams in comparison with the angles that were used in our experiments.

The results obtained are planned to be used in the future for processing thin films of light-sensitive materials in order to study the influence of the polarization of generated periodically repeating light fields on the structure of manufactured nano- and microstructures [25] and for parallel laser manipulation of multiple nano- and micro-objects. In the

field of laser processing of materials, the use of multi-beam interference patterns makes it possible to achieve high efficiency and quality in the manufacture of arrays of the desired nano- and microelements. As we have shown in this work, controlling the polarization states of interfering beams leads to the generation of light fields with different polarization distributions, which can be visualized in some photosensitive materials. In this case, the amplitude distributions of the generated interference patterns can have the same structure. Thus, only by controlling the polarization states of individual beams in a superposition can one significantly change the polarization structure of the generated light fields and the structure of the patterns recorded in photosensitive materials. This is very convenient, especially when using multi-stage laser processing, since it allows online control of the profiles of manufactured structures. In the field of laser manipulation, such SAM distributions can also be used to implement micropumps and study the hydrodynamic interactions of numerous optically trapped nano- and microparticles. Research into these interactions will contribute to biological sciences and nanotechnology [64–67].

Author Contributions: Conceptualization, S.N.K., A.V.U. and A.P.P.; methodology, S.N.K., S.V.K. and A.V.U.; software, S.N.K.; validation, A.P.P. and S.N.K.; formal analysis, A.V.U.; investigation, S.N.K. and A.P.P.; resources, S.N.K., S.V.K. and A.P.P.; data curation, S.N.K. and A.P.P.; writing—original draft preparation, S.N.K., A.V.U., S.V.K. and A.P.P.; writing—review and editing, S.N.K. and A.P.P.; visualization, S.N.K. and A.P.P.; supervision, S.N.K.; project administration, S.N.K. and S.V.K.; funding acquisition, S.V.K. and A.P.P. All authors have read and agreed to the published version of the manuscript.

Funding: This work was supported by the Russian Science Foundation, project no. 22-12-00041 (in part of theoretical analysis, numerical calculations, and experimental investigation of four-beam cases), and within the State Assignment of the NRC “Kurchatov Institute” (as part of theoretical analysis and numerical calculations of two-beam cases).

Institutional Review Board Statement: Not applicable.

Informed Consent Statement: Not applicable.

Data Availability Statement: Data underlying the results presented in this paper are not publicly available at this time but may be obtained from the authors upon reasonable request.

Conflicts of Interest: The authors declare no conflicts of interests.

References

1. Forbes, A. Structured light from lasers. *Laser Photonics Rev.* **2019**, *13*, 1900140. [[CrossRef](#)]
2. Fu, P.; Ni, P.N.; Wu, B.; Pei, X.Z.; Wang, Q.H.; Chen, P.P.; Xu, C.; Kan, Q.; Chu, W.G.; Xie, Y.Y. Metasurface enabled on-chip generation and manipulation of vector beams from vertical cavity surface-emitting lasers. *Adv. Mater.* **2023**, *35*, 2204286. [[CrossRef](#)] [[PubMed](#)]
3. Skoulas, E.; Manousaki, A.; Fotakis, C.; Stratakis, E. Biomimetic surface structuring using cylindrical vector femtosecond laser beams. *Sci. Rep.* **2017**, *7*, 45114. [[CrossRef](#)] [[PubMed](#)]
4. Rosales-Guzmán, C.; Ndagano, B.; Forbes, A. A review of complex vector light fields and their applications. *J. Opt.* **2018**, *20*, 123001. [[CrossRef](#)]
5. Stafeev, S.S.; Kotlyar, V.V.; Nalimov, A.G.; Kotlyar, M.V.; O’Faolain, L. Subwavelength gratings for polarization conversion and focusing of laser light. *Photonics Nanostruct.-Fundam. Appl.* **2017**, *27*, 32–41. [[CrossRef](#)]
6. Wen, D.; Crozier, K.B. Metasurfaces 2.0: Laser-integrated and with vector field control. *APL Photonics* **2021**, *6*, 080902. [[CrossRef](#)]
7. Khonina, S.N.; Butt, M.A.; Kazanskiy, N.L. A Review on Reconfigurable Metalenses Revolutionizing Flat Optics. *Adv. Opt. Mater.* **2023**, *12*, 2302794. [[CrossRef](#)]
8. Maurer, C.; Jesacher, A.; FÜRhapter, S.; Bernet, S.; Ritsch-Marte, M. Tailoring of arbitrary optical vector beams. *New J. Phys.* **2007**, *9*, 78. [[CrossRef](#)]
9. Khonina, S.N.; Porfirev, A.P. Harnessing of inhomogeneously polarized Hermite–Gaussian vector beams to manage the 3D spin angular momentum density distribution. *Nanophotonics* **2021**, *11*, 697–712. [[CrossRef](#)]
10. Khonina, S.N.; Karpeev, S.V. Grating-based optical scheme for the universal generation of inhomogeneously polarized laser beams. *Appl. Opt.* **2010**, *49*, 1734–1738. [[CrossRef](#)]
11. Khonina, S.N.; Karpeev, S.V.; Porfirev, A.P. Sector sandwich structure: An easy-to-manufacture way towards complex vector beam generation. *Opt Express* **2020**, *28*, 27628–27643. [[CrossRef](#)] [[PubMed](#)]

12. Uesugi, Y.; Miwa, T.; Kadoguchi, N.; Kozawa, Y.; Sato, S. Multi-beam ultrafast laser processing of free-standing nanofilms. *Appl. Phys. A* **2023**, *129*, 101. [[CrossRef](#)]
13. Yang, Y.; Ren, Y.X.; Chen, M.; Arita, Y.; Rosales-Guzmán, C. Optical trapping with structured light: A review. *Adv. Photonics* **2021**, *3*, 034001. [[CrossRef](#)]
14. Kim, D.Y.; Tripathy, S.K.; Li, L.; Kumar, J. Laser-induced holographic surface relief gratings on nonlinear optical polymer films. *Appl. Phys. Lett.* **1995**, *66*, 1166–1168. [[CrossRef](#)]
15. Yu, F.; Li, P.; Shen, H.; Mathur, S.; Lehr, C.-M.; Bakowsky, U.; Mücklich, F. Laser interference lithography as a new and efficient technique for micropatterning of biopolymer surface. *Biomaterials* **2005**, *26*, 2307–2312. [[CrossRef](#)] [[PubMed](#)]
16. Lai, N.D.; Liang, W.P.; Lin, J.H.; Hsu, C.C.; Lin, C.H. Fabrication of two- and three-dimensional periodic structures by multi-exposure of two-beam interference technique. *Opt. Express* **2005**, *13*, 9605–9611. [[CrossRef](#)] [[PubMed](#)]
17. Xia, D.; Ku, Z.; Lee, S.C.; Brueck, S.R.J. Nanostructures and functional materials fabricated by interferometric lithography. *Adv. Mater.* **2011**, *23*, 147–179. [[CrossRef](#)] [[PubMed](#)]
18. Vala, M.; Homola, J. Multiple beam interference lithography: A tool for rapid fabrication of plasmonic arrays of arbitrary shaped nanomotifs. *Opt. Express* **2016**, *24*, 15656–15665. [[CrossRef](#)]
19. Rebollar, E.; Castillejo, M.; Ezquerra, T.A. Laser induced periodic surface structures on polymer films: From fundamentals to applications. *Eur. Polym. J.* **2015**, *73*, 162–174. [[CrossRef](#)]
20. Porfirev, A.P.; Khonina, S.N.; Meshalkin, A.; Ivliev, N.A.; Achimova, E.; Abashkin, V.; Prisacar, A.; Podlipnov, V.V. Two-step maskless fabrication of compound fork-shaped gratings in nanomultilayer structures based on chalcogenide glasses. *Opt. Lett.* **2021**, *46*, 3037–3040. [[CrossRef](#)]
21. Gorkhali, S.P.; Cloutier, S.G.; Crawford, G.P.; Pelcovits, R.A. Stable polarization gratings recorded in azo-dyedoped liquid crystals. *Appl. Phys. Lett.* **2006**, *88*, 251113. [[CrossRef](#)]
22. Wang, D.; Wang, Z.; Zhang, Z.; Yue, Y.; Li, D.; Maple, C. Effects of polarization on four-beam laser interference lithography. *Appl. Phys. Lett.* **2016**, *102*, 081903. [[CrossRef](#)]
23. Achimova, E.; Stronski, A.; Abashkin, V.; Meshalkin, A.; Paiuk, A.; Prisacar, A.; Oleksenko, P.; Triduh, G. Direct surface relief formation on As₂S₃-Se nanomultilayers in dependence on polarization states of recording beams. *Opt. Mater.* **2015**, *47*, 566. [[CrossRef](#)]
24. Meshalkin, A.; Losmanschii, C.; Prisacar, A.; Achimova, E.; Abashkin, V.; Pogrebnoi, S.; Macaev, F. Carbazole-based azopolymers as media for polarization holographic recording. *Adv. Phys. Res.* **2019**, *1*, 86–98.
25. Porfirev, A.P.; Khonina, S.N.; Ivliev, N.A.; Fomchenkov, S.A.; Porfirev, D.P.; Karpeev, S.V. Polarization-sensitive patterning of azopolymer thin films using multiple structured laser beams. *Sensors* **2023**, *23*, 112. [[CrossRef](#)] [[PubMed](#)]
26. Sakamoto, M.; Kaneko, Y.; Nakamoto, Y.; Noda, K.; Sasaki, T.; Kawatsuki, N.; Ono, H. Mode demultiplexing of vector beams using crossed-fork-shaped polarization grating fabricated by photoalignment of photo-crosslinkable liquid crystal polymer. *Appl. Phys. Lett.* **2019**, *115*, 061104. [[CrossRef](#)]
27. Stay, J.L.; Gaylord, T.K. Three-beam-interference lithography: Contrast and crystallography. *Appl. Opt.* **2008**, *47*, 3221–3230. [[CrossRef](#)]
28. He, J.; Fang, X.; Lin, Y.; Zhang, X. Polarization control in flexible interference lithography for nano-patterning of different photonic structures with optimized contrast. *Opt. Express* **2015**, *23*, 11518. [[CrossRef](#)] [[PubMed](#)]
29. Miller, D.B.; Jones, A.; McLeod, R.R. Contrast analysis in two-beam laser interference lithography. *Appl. Opt.* **2020**, *59*, 5399–5407. [[CrossRef](#)]
30. Peng, F.; Du, J.; Du, J.; Wang, S.; Yan, W. Contrast analysis of polarization in three-beam interference lithography. *Appl. Sci.* **2021**, *11*, 4789. [[CrossRef](#)]
31. Richards, B.; Wolf, E. Electromagnetic diffraction in optical systems, II. Structure of the image field in an aplanatic system. *Proc. R. Soc. Lond. Ser. A Math. Phys. Sci.* **1959**, *253*, 358–379.
32. Khonina, S.N. Vortex beams with high-order cylindrical polarization: Features of focal distributions. *Appl. Phys. B* **2019**, *125*, 100. [[CrossRef](#)]
33. Born, M.; Wolf, E. *Principles of Optics*, 6th ed.; Pergamon: Oxford, UK, 1980.
34. Cai, L.Z.; Yang, X.L. Interference of circularly polarized light: Contrast and application in fabrication of three-dimensional periodic microstructures. *Opt. Laser Technol.* **2002**, *34*, 671–674. [[CrossRef](#)]
35. Burrow, G.M.; Gaylord, T.K. Multi-beam interference advances and applications: Nano-electronics, photonic crystals, metamaterials, subwavelength structures, optical trapping, and biomedical structures. *Micromachines* **2011**, *2*, 221–257. [[CrossRef](#)]
36. Xiao, Y.; Zhang, Y.; Shi, Y.; Jiang, S. The study on optical lattice formed by four-beam interference. *Optik* **2016**, *127*, 10421–10427. [[CrossRef](#)]
37. Wang, L.; Wang, Z.-H.; Yu, Y.-H.; Sun, H.-B. Laser interference fabrication of large-area functional periodic structure surface. *Front. Mech. Eng.* **2018**, *13*, 493–503. [[CrossRef](#)]
38. Shimizu, Y. Laser Interference Lithography for Fabrication of Planar Scale Gratings for Optical Metrology. *Nanomanuf. Metrol.* **2021**, *4*, 3–27. [[CrossRef](#)]
39. Sekkat, Z.; Kawata, S. Laser nanofabrication in photoresists and azopolymers. *Laser Photonics Rev.* **2014**, *8*, 1–26. [[CrossRef](#)]
40. Meier, M.; Romano, V.; Feurer, T. Material processing with pulsed radially and azimuthally polarized laser radiation. *Appl. Phys. A* **2007**, *86*, 329–334. [[CrossRef](#)]

41. Danilov, P.A.; Saraeva, I.N.; Kudryashov, S.I.; Porfirev, A.P.; Kuchmizhak, A.A.; Zhizhchenko, A.Y.; Rudenko, A.A.; Umanskaya, S.F.; Zayarny, D.A.; Ionin, A.A.; et al. Polarization-selective excitation of dye luminescence on a gold film by structured ultrashort laser pulses. *JETP Lett.* **2018**, *107*, 15–18. [[CrossRef](#)]
42. Zhai, Y.; Cao, L.; Liu, Y.; Tan, X. A review of polarization-sensitive materials for polarization holography. *Materials* **2020**, *13*, 5562. [[CrossRef](#)] [[PubMed](#)]
43. Porfirev, A.; Khonina, S.; Ivliev, N.; Meshalkin, A.; Achimova, E.; Forbes, A. Writing and reading with the longitudinal component of light using carbazole-containing azopolymer thin films. *Sci. Rep.* **2022**, *12*, 3477. [[CrossRef](#)] [[PubMed](#)]
44. Priimagi, A.; Shevchenko, A. Azopolymer-Based Micro-and Nanopatterning for Photonic Applications. *J. Polym. Sci. B Polym. Phys.* **2014**, *52*, 163–182. [[CrossRef](#)]
45. Vladimirov, V.S. *Methods of the Theory of Generalized Functions*; Taylor & Francis: London, UK, 2002.
46. Vaz, J., Jr. Some comments on integrals involving the Dirac delta function. *Rev. Bras. Ensino Fis.* **2022**, *44*, e20210378. [[CrossRef](#)]
47. Bekshaev, A. Dynamical characteristics of electromagnetic field under conditions of total internal reflection. *J. Opt.* **2018**, *4*, 045604. [[CrossRef](#)]
48. Holbourn, A. Angular Momentum of Circularly Polarised Light. *Nature* **1936**, *137*, 31. [[CrossRef](#)]
49. Garcés-Chávez, V.; McGloin, D.; Padgett, M.J.; Dultz, W.; Schmitzer, H.; Dholakia, K. Observation of the transfer of the local angular momentum density of a multiringed light beam to an optically trapped particle. *Phys. Rev. Lett.* **2003**, *91*, 093602. [[CrossRef](#)]
50. Li, M.; Yan, S.; Yao, B.; Liang, Y.; Zhang, P. Spinning and orbiting motion of particles in vortex beams with circular or radial polarizations. *Opt. Express* **2016**, *24*, 20604–20612. [[CrossRef](#)] [[PubMed](#)]
51. Zhang, Y.; Xue, Y.; Zhu, Z.; Rui, G.; Cui, Y.; Gu, B. Theoretical investigation on asymmetrical spinning and orbiting motions of particles in a tightly focused power-exponent azimuthal-variant vector field. *Opt. Express* **2018**, *26*, 4318–4329. [[CrossRef](#)]
52. Bliokh, K.Y.; Nori, F. Transverse spin of a surface polariton. *Phys. Rev. A* **2012**, *85*, 061801. [[CrossRef](#)]
53. Banzer, P.; Neugebauer, M.; Aiello, A.; Marquardt, C.; Lindlein, N.; Bauer, T.; Leuchs, G. The photonic wheel-demonstration of a state of light with purely transverse angular momentum. *J. Eur. Opt. Soc.* **2013**, *8*, 13032. [[CrossRef](#)]
54. Aiello, A.; Banzer, P.; Neugebauer, M.; Leuchs, G. From transverse angular momentum to photonic wheels. *Nat. Photonics* **2015**, *9*, 789. [[CrossRef](#)]
55. Bliokh, K.Y.; Nori, F. Transverse and longitudinal angular momenta of light. *Phys. Rep.* **2015**, *592*, 1. [[CrossRef](#)]
56. Khonina, S.N.; Ustinov, A.V.; Porfirev, A.P. Vector Lissajous laser beams. *Opt. Lett.* **2020**, *45*, 4112–4115. [[CrossRef](#)]
57. Ralston, J. Gaussian beams and the propagation of singularities. *Studies in Partial Differential Equations. MAA Stud. Math.* **1983**, *23*, 206–248.
58. Motamed, M.; Runborg, O. A wavefront-based Gaussian beam method for computing high frequency wave propagation problems. *Comput. Math. Appl.* **2015**, *69*, 949–963. [[CrossRef](#)]
59. Meshalkin, A.; Robu, S.; Achimova, E.; Prisacar, A.; Shepel, D.; Abaskin, V.; Triduh, G. Direct photoinduced surface relief formation in carbazole-based azopolymer using polarization holographic recording. *J. Optoelectron. Adv. Mater.* **2016**, *18*, 763–768.
60. Ivliev, N.A.; Khonina, S.N.; Podlipnov, V.V.; Karpeev, S.V. Holographic Writing of Forked Diffraction Gratings on the Surface of a Chalcogenide Glass Semiconductor. *Photonics* **2023**, *10*, 125. [[CrossRef](#)]
61. Kulikovska, O.; Gharagozloo-Hubmann, K.; Stumpe, J.; Huey, B.D.; Bliznyuk, V.N. Formation of surface relief grating in polymers with pendant azobenzene chromophores as studied by AFM/UFM. *Nanotechnology* **2012**, *23*, 485309. [[CrossRef](#)]
62. Rao, L.; Pu, J.; Chen, Z.; Yei, P. Focus shaping of cylindrically polarized vortex beams by a high numerical-aperture lens. *Opt. Laser Technol.* **2009**, *41*, 241–246. [[CrossRef](#)]
63. Zhou, Z.-H.; Guo, Y.-K.; Zhu, L.-Q. Tight focusing of axially symmetric polarized vortex beams. *Chin. Phys. B* **2014**, *23*, 044201. [[CrossRef](#)]
64. Freitas Carvalho, F.; Augusto de Moraes Cruz, C.; Costa Marques, G.; Martins Cruz Damasceno, K. Angular Light, Polarization and Stokes Parameters Information in a Hybrid Image Sensor with Division of Focal Plane. *Sensors* **2020**, *20*, 3391. [[CrossRef](#)] [[PubMed](#)]
65. Ruh, D.; Tränkle, D.; Rohrbach, A. Fast parallel interferometric 3D tracking of numerous optically trapped particles and their hydrodynamic interaction. *Opt. Express* **2011**, *19*, 21627. [[CrossRef](#)] [[PubMed](#)]
66. Tsuji, T.; Nakatsuka, R.; Nakajima, K.; Doi, K.; Kawano, S. Effect of hydrodynamic inter-particle interaction on the orbital motion of dielectric nanoparticles driven by an optical vortex. *Nanoscale* **2020**, *12*, 6673. [[CrossRef](#)]
67. Ghosh, R.; Bentil, S.A.; Jaurez, J.J. Particle-wall hydrodynamic effects on optical trapping viscometry. *Colloids Surf. A Physicochem. Eng. Asp.* **2024**, *682*, 132942. [[CrossRef](#)]

Disclaimer/Publisher's Note: The statements, opinions and data contained in all publications are solely those of the individual author(s) and contributor(s) and not of MDPI and/or the editor(s). MDPI and/or the editor(s) disclaim responsibility for any injury to people or property resulting from any ideas, methods, instructions or products referred to in the content.